Thermal decoherence of superradiance in lead halide perovskite nanocrystal superlattices

Francesco Mattiotti,[*,†,‡,¶] Masaru Kuno,[†,§] Fausto Borgonovi,[‡,¶] Boldizsár Jankó,[†] and G. Luca Celardo[∥]

†*Department of Physics, University of Notre Dame, Notre Dame, IN, USA*
‡*Dipartimento di Matematica e Fisica and Interdisciplinary Laboratories for Advanced Materials Physics, Università Cattolica del Sacro Cuore, Brescia, Italy*
¶*Istituto Nazionale di Fisica Nucleare, Sezione di Pavia, Pavia, Italy*
§*Department of Chemistry and Biochemistry, University of Notre Dame, Notre Dame, IN, USA*
∥*Benemérita Universidad Autónoma de Puebla, Instituto de Física, Puebla, Mexico*

E-mail: fmattiot@nd.edu

Abstract

Recent experiments by Rainò et al.[1] have documented cooperative emission from $CsPbBr_3$ nanocrystal superlattices, exhibiting the hallmarks of low temperature superradiance. In particular, the optical response is coherent and the radiative decay rate is increased by a factor of three, relative to that of individual nanocrystals. However, the increase is six orders of magnitude smaller than what is theoretically expected from the superradiance of large assemblies, consisting of 10^6 to 10^8 interacting nanocrystals. Here we develop a theoretical model of superradiance for such systems and show that thermal decoherence is largely responsible for the drastic reduction of the radiative decay rate in nanocrystal superlattices. Our theoretical approach explains the experimental results[1] and provides insight into the design of small nanocrystal superlattices, able to show a four orders of magnitude enhancement in superradiant response. These quantitative predictions pave the path towards observing superradiance at higher temperatures.

Keywords

Cooperative effects, superradiance, superfluorescence, quantum materials, quantum dots, $CsPbBr_3$, perovskite, nanocrystals, superlattice

Spontaneous emission is a basic quantum mechanical effect due to the coupling of an excited electronic state with the vacuum state of the electromagnetic field. In an ensemble of identical emitters, cooperative radiation emerges. Called superfluorescence,[2] or superradiance (SR) by Dicke, who first proposed the phenomenon in 1954,[3] this effect arises from the excitation of an ensemble of individual dipole emitters and results in an emissive, macroscopic quantum state. SR has been observed in a variety of systems,[4] with some of the most recent examples being cold atomic clouds,[5] photosynthetic antenna complexes,[6] molecular aggregates,[7,8] quantum dots[9,10] and nitrogen vacancies in nanodiamonds.[11] This effect is relevant in enhancing absorption and energy transfer, which has been proposed to improve the efficiency of light-harvesting systems.[12–16] SR also leads to spectrally ultranarrow laser beams.[17]

In an exciting new development, SR-like behavior has recently been observed at low temperature ($T = 6$ K) in a solid state superlattice of $CsPbBr_3$ perovskite nanocrystals (NCs).[1] These superlattices consist of $\sim 10^6 - 10^8$ individual cubic NCs self-assembled into ordered cubic arrays with dimensions on the order of microns. Lead halide perovskite NC superlattices distinguish themselves from analogous semiconductor NC superlattices[18,19] in that $CsPbBr_3$ NCs have very high emission quantum yields and very short radiative lifetimes.[20] This high sensitivity to incoming photons makes $CsPbBr_3$ NCs ideal candidates for building photon sensors and quantum devices. For this reason, recent experimental evidence of SR in $CsPbBr_3$ NC superlattices[1] represents an exciting development.

Apparent $CsPbBr_3$ NC superlattice SR distinguishes itself from the normal band edge emission of $CsPbBr_3$ NCs in that it exhibits a 2.7 times faster radiative lifetime. Most importantly, the emission is coherent as seen through first- and second-order correlation measurements.

Despite these highly suggestive results, there are notable discrepancies in the experimental observations[1] from what is expected of SR behavior. Our primary concern is the reported 2.7 times radiative rate enhancement. This is because SR radiative rate enhancements scale as N, the number of interacting dipoles.[2,4,21] Given that there are approximately $N \sim 10^6 - 10^8$ NC emitters in the superlattice, the observed factor of 2.7 enhancement easily differs by six orders of magnitude from what is expected at low temperature (6 K). For instance, at similar temperatures, SR enhancement in molecular systems is hundreds of times larger.[7,8]

We have now developed an open quantum model,[24] based on the use of well-known non-Hermitian radiative Hamiltonians,[25] to rationalize SR-like emission from NC superlattices in the weak excitation regime. Our model specifically applies to the low fluence (500 nJ cm^{-2}) fluorescence measurements of Ref. 1 (see **Supporting Information, section S1**). This regime is also relevant for renewable energy ap-

plications, involving light harvesting, and has previously been invoked when modeling the SR of molecular aggregates[25] and cold atom gases.[22,26]

We model the $CsPbBr_3$ NC band edge electronic structure using a four-level system, which accounts for the main isotropic $s - p$ transitions of single NCs.[20] In the low fluence regime, we limit our considerations to the single excitation manifold, spanned by the states $|n, \alpha\rangle = \hat{a}_{n,\alpha}^\dagger |G\rangle$, where one excitation is present on the $\alpha = x, y, z$ state of the nth NC, while all the other NCs are in their ground states. Here, $|G\rangle$ is the ground state of the whole system, where no excitation is present, and $\hat{a}_{n,\alpha}^\dagger$ is an operator that creates an excitation on the αth state of the nth NC. The label $\alpha = x, y, z$ denotes the three angular momentum states of the p orbital. In our simulations, we consider an ensemble of N NCs, each of edge length l, forming a cubic superlattice of edge length $L \gg l$. The center-to-center distance between neighboring NCs is $l' = l + b$, which accounts for the presence of surface ligands. In our simulations, $b = 1$ nm, as commonly seen in superlattices.[27]

The following $3N \times 3N$ non-Hermitian, radiative Hamiltonian

$$
\begin{aligned}
\hat{H} = &\sum_{n=1}^{N} \sum_{\alpha=x,y,z} E_n |n, \alpha\rangle \langle n, \alpha| \\
&+ \sum_{\alpha,\beta} \sum_{n \neq m} J_{mn}^{\alpha\beta} |m, \alpha\rangle \langle n, \beta| \qquad (1a)
\end{aligned}
$$

accounts for interactions between individual NCs and their common light field[22,25] where point-dipole couplings have been implicitly assumed (see **Supporting Information, section S2**). Furthermore, $E_n = \hbar \left(\omega_0 - i\frac{\gamma_r}{2} \right)$ is the complex self-energy of the nth NC, where $\hbar\omega_0 = 2.38$ eV is the NC transition energy[1] and $\gamma_r = \mu^2 \omega_0^3 \sqrt{\epsilon_r} / (3\pi\epsilon_0 \hbar c^3) = 2.5$ ns^{-1} is the radiative decay rate of a single NC[1] (with $\mu = 23$ D being the single NC transition dipole moment, $\epsilon_r = 4.8$ the relative dielectric permittivity at frequency ω_0,[20] ϵ_0 the vacuum permittivity and c the speed of light). Moreover, $J_{mn}^{\alpha\beta} = \Omega_{mn}^{\alpha\beta} - \frac{i}{2}\Gamma_{mn}^{\alpha\beta}$ with the real and imaginary
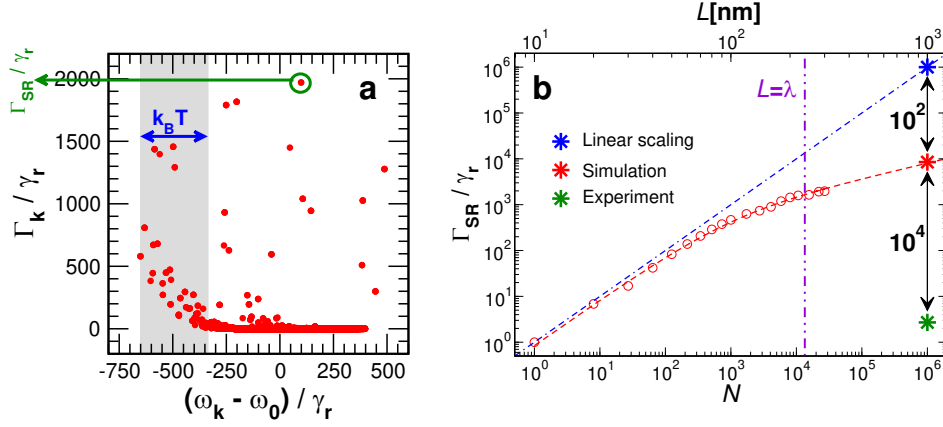
Figure 1: **a** Eigenvalues in the complex plane of the Hamiltonian $\hat{H}$ (see Eq. (1a)) for a cubic superlattice of $N = 30^3$ NCs. $\hat{H}$ has dimensions $3N \times 3N = 6.561 \times 10^9$. The SR rate, Γ_{SR}, corresponding to the maximal decay rate, is circled green. The grayed region denotes the energy range within $k_B T$ of the ground state energy at $T = 6$ K. **b** Plot of Γ_{SR}/γ_r versus N. The dashed blue line represents the maximal SR rate theoretically achievable. The violet vertical dash-dotted line indicates where L equals the wavelength λ of emitted light within the material. Simulation data (circles) have been fit (dashed red line) to the function $\Gamma_{SR}/\gamma_r = CN/(N^{2/3} + N_{cr}^{2/3})$ (fit parameters: $C = 81.2$ and $N_{cr} = 932$), that interpolates between the $\sim N$ behavior (expected for $L \ll \lambda$) and $\sim N^{1/3}$ (expected for $L \gtrsim \lambda$).[22,23] The green symbol marks the experimental results of Ref. 1. Parameters for **a,b**: single NC radiative lifetime $1/\gamma_r = \tau_r = 0.4$ ns, single NC band edge energy $\hbar\omega_0 = 2.38$ eV, relative dielectric constant at optical frequencies $\epsilon_r = 4.8$ and NC edge length, $l = 9$ nm.

parts given by

$$\Omega_{mn}^{\alpha\beta} = \frac{\hbar\gamma_r}{2}\left\{ y_0\left(k_0 r_{mn}\right)\hat{e}_\alpha \cdot \hat{e}_\beta \right. \tag{1b}$$
$$\left. -\frac{y_2\left(k_0 r_{mn}\right)}{2}\left[\hat{e}_\alpha \cdot \hat{e}_\beta - 3\left(\hat{e}_\alpha \cdot \hat{r}_{mn}\right)\left(\hat{e}_\beta \cdot \hat{r}_{mn}\right)\right]\right\},$$

$$\Gamma_{mn}^{\alpha\beta} = \hbar\gamma_r\left\{ j_0\left(k_0 r_{mn}\right)\hat{e}_\alpha \cdot \hat{e}_\beta \right. \tag{1c}$$
$$\left. -\frac{j_2\left(k_0 r_{mn}\right)}{2}\left[\hat{e}_\alpha \cdot \hat{e}_\beta - 3\left(\hat{e}_\alpha \cdot \hat{r}_{mn}\right)\left(\hat{e}_\beta \cdot \hat{r}_{mn}\right)\right]\right\}.$$

Here, $y_0(x)$, $y_2(x)$, $j_0(x)$, and $j_2(x)$ are spherical Bessel functions, $k_0 = \omega_0\sqrt{\epsilon_r}/c$ is the transition wavenumber, $\hat{e}_\alpha$ is the unit vector along the α direction, r_{mn} is the distance between the mth and nth NC and $\hat{r}_{mn}$ is the unit vector joining them. $J_{mn}^{\alpha\beta}$ describes the full radiative coupling between different NC transition dipoles in the superlattice.

A similar approach has recently been proposed to model two-dimensional CsPbBr$_3$ NC superlattices.[28] The employed dipolar near-field coupling, however, is not valid for distances larger than λ, the NC band edge transition

wavelength inside the material. This means that collective radiation cannot be analyzed for typical experimental system sizes where $L \approx 5\lambda$ (see **Supporting Information, section S1**). Within our approach interference between different emitters is implicitly accounted for by $J_{mn}^{\alpha\beta}$ even for distances larger than λ. Diagonalizing $\hat{H}$, in turn, yields complex eigenenergies $E_k = \hbar\left(\omega_k - i\frac{\Gamma_k}{2}\right)$ where the imaginary part is related to the radiative lifetime $\tau_k = \Gamma_k^{-1}$ of the kth eigenstate.

Figure 1a shows the typical complex spectrum for a superlattice of $N = 30^3 = 27,000$ NCs with individual NC edge lengths of $l = 9$ nm and an associated center-to-center distance of $l' = 10$ nm. Here both the decay widths ($\hbar\Gamma_k$) and the real energies ($\hbar\omega_k$) are normalized with the single NC decay width $\hbar\gamma_r \approx 1.6$ μeV. We identify the SR decay, Γ_{SR}, as the maximal decay rate predicted (cf. circle in **Figure 1a**), since time evolution from a generic initial state is dominated by $\sim \exp(-\Gamma_{SR}t)$, assuming $T = 0$ K (see **Supporting Information, section S3**). Note
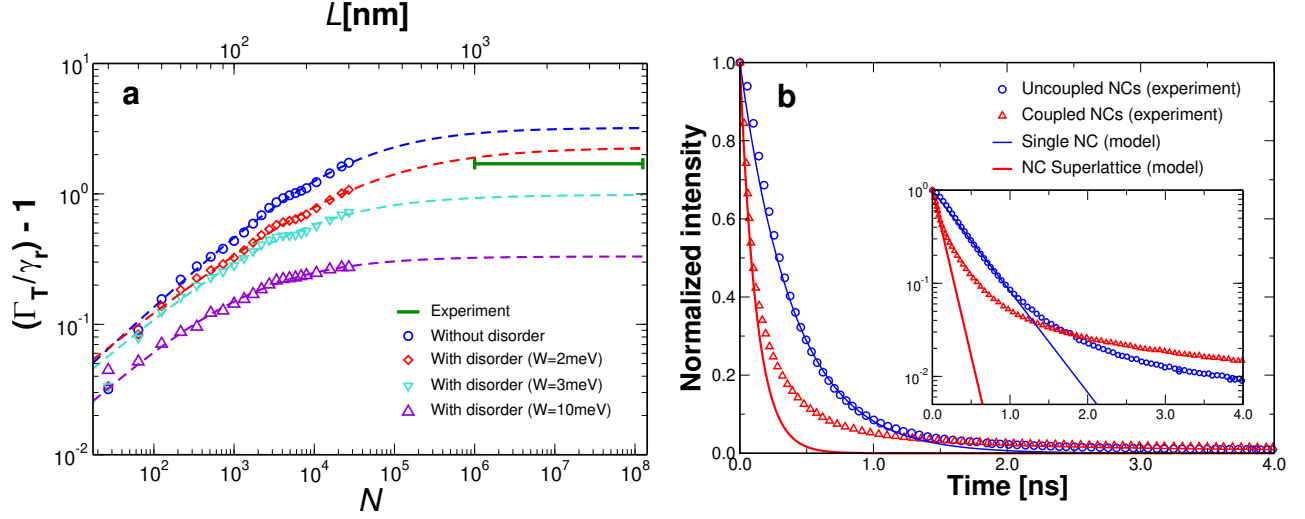
3

Figure 2: **a** Thermal average of the normalized radiative decay, $(\Gamma_T/\gamma_r) - 1$, (Eq. (2)) versus N. Note that we subtract one from the normalized thermal radiative rate to improve the visibility at small decay rates. The 2.7 enhancement reported in Ref. 1 is shown in solid green. Symbols are obtained from numerical diagonalization of Eq. (1a). Dashed lines are best fits using the function $(\Gamma_T/\gamma_r) - 1 = AN^B/(N^B + N_{sat}^B)$, with fit parameters A, B, N_{sat} (values in **Supporting Information, section S6**). **b** Comparison of the experimental[1] NC superlattice SR radiative decay rate to theory, accounting for thermalization and static disorder ($W = 2$ meV). Temperature is 6 K. "Coupled NCs" refers to the decay of coupled NCs in a superlattice, while "Uncoupled NCs" refers to the measured decay of isolated, non-interacting NCs. Inset: same data on a logarithmic y-scale. In both **a,b**, $\hbar\omega_0 = 2.38$ eV, $\gamma_r = 2.5$ ns^{-1}, $\epsilon_r = 4.8$ and $l = 9$ nm.

that the energy of the maximal SR state is highly dependent on the superlattice geometry, dimension and on the ratio L/λ, see **Supporting information, section S4.**

Given that the system size we consider, $N = 30^3$, is two orders of magnitude smaller than that used experimentally[1] ($N \sim 10^6 - 10^8$), we study how Γ_{SR} scales with N and extrapolate its value to experimentally-relevant superlattice sizes using the well-established relationship:[22,23] $\Gamma_{SR} \propto N$ for $L \ll \lambda$ and $\Gamma_{SR} \propto N/(L/\lambda)^2$ for for $L \gtrsim \lambda$, which implies $\Gamma_{SR} \propto N^{1/3}$ for a fixed NC superlattice density of N/L^3.

By extrapolating Γ_{SR} to large N, our model predicts a SR lifetime of order $\tau_{SR} \sim 0.04$ ps for a NC superlattice of similar size to the one studied experimentally[1] (see **Figure 1b** and **Supporting Information, section S3**). Thus we predict at least $\Gamma_{SR}/\gamma_r \sim 10^4$ for the experimental NC and superlattice size, which is four orders of magnitude larger than the enhancement observed in Ref. 1.

At this point, we suggest that what prevents agreement between theory and experiment is the absence of an explicit consideration of the sensitivity of SR to thermalization-induced coherence losses and structural disorder. Indeed, thermal noise suppresses quantum coherence, especially when $k_B T$ becomes comparable to the spectral width of the interacting ensemble (typically of the same order as the nearest-neighbor coupling J). This can lead to highly suppressed SR in the regime experimentally investigated,[1] since at 6 K $k_B T = 0.5$ meV, which is ~ 3 times larger than the estimated $J = 0.14$ meV coupling between nearest NC neighbors.

We therefore account for thermalization effects on NC superlattice SR by taking thermal averages of all superradiant and subradiant eigenstate emission rates,[29,30] namely

$$\Gamma_T = \frac{1}{Z} \sum_k \Gamma_k e^{-\hbar\omega_k/(k_B T)} , \qquad (2)$$

where $Z = \sum_k e^{-\hbar\omega_k/(k_B T)}$ is the partition func-

4

tion. From Equation (2), a corresponding emission intensity is $I(t) \propto \exp(-\Gamma_T t)$, with Γ_T the thermal decay rate. Thermalization therefore suppresses SR so that $\Gamma_T \approx \gamma_r$ (with $\gamma_r = \tau_r^{-1}$) if $k_B T$ is comparable to the spectral width of the coupled system. Note that in using Equation (2) we implicitly assume that thermal relaxation dominates all other relaxation processes in the material (see details in **Supporting Information, section S5**).

Figure 2a shows that by taking thermal averages for different superlattice sizes (blue circles), we observe an initial fast increase of Γ_T for small N, followed by a slower increase at large N. Assuming saturation in the limit $N \to \infty$ (see **Supporting Information, section S7**), we estimate $\Gamma_T/\gamma_r \approx 4.2$ for $N \sim 10^6 - 10^8$. This is in excellent agreement with the experimental results[1] where $\Gamma_{EXP}/\gamma_r \approx 2.7$.

An even better correspondence is found by taking into account structural disorder in the superlattice, stemming from NC size heterogeneities[1,31] as well as inhomogeneities in NC positions and orientations. To estimate the impact this structural disorder has on SR, we consider excitation energy fluctuations, which we model by adding an on-site disorder of strength W (see also **Supporting Information, section S8**). This form of disorder has previously been used[32] to model the effects of different sources of time-independent disorder in various systems.

By introducing such disorder and extrapolating the results to experimentally-relevant superlattice sizes, we find excellent agreement with experiment[1] for W between 2 meV and 3 meV, see **Figure 2a** where the experimental[1] result is shown in green. Note these values of W are several times larger than the nearest-neighbor coupling $J = 0.14$ meV ($W/J \approx 15$).

Figure 2b now compares the theoretical decay, Γ_T, for $W = 2$ meV (red line) to the experimental emission intensity decay reported in Ref. 1 (red triangles). Our theoretical emission intensity accounts for $\sim 70\%$ of the experimental intensity decay. A discrepancy between theory and experiment is visible at long times (see also inset). This likely reflects omissions in the theory, namely not accounting for

non-radiative processes in NCs that lead to non-unity emission quantum yields.[33] This interpretation is confirmed by the non-exponential decay of the emission from an ensemble of uncoupled NCs (blue circles, **Figure 2b**). Modelling such processes is highly non trivial since they should account for dynamical transitions between radiative and non-radiative channels, possibly including activation/deactivation processes for non-radiative channels that induce blinking.[34,35] At this point, however, our proposed theoretical framework, which accounts for thermalization and structural disorder, generally rationalizes the superradiant accelerated PL decay reported in Ref. 1.

In Ref. 1 it was also observed that the emission spectrum of single superlattices consists of several emission peaks, with the SR emission band being redshifted relative to the emission of uncoupled NCs by 64 ± 6 meV (an average across 10 superlattices). This redshift cannot be explained by dipolar couplings between NCs in our model, which at best induces a few meV redshift to the SR emission, see **Supporting Information, section S9.**

While the origin of a redshifted emission from superlattices remains debated,[36–42] (see **Supporting Information, section S9.**), we conjecture here that the SR redshifted emission observed in Ref. 1 arises from the existence of sub-domains, composed of larger NCs, within individual superlattices. In fact, this has already been suggested by the authors of Ref. 1. Supporting this are $CsPbBr_3$ NC size-dependent band energies that change by hundreds of meV when NC edge lengths change from $l = 3$ nm to $l = 12.8$ nm.[31] Consequently, large NC SR-active sub-domains will show a sizable redshift relative to uncoupled and smaller NCs present in the same NC superlattice. It is of note that larger NCs have an inherently higher likelihood of realizing uniform SR-active sub-domains, due to their smaller relative edge length fluctuations,[31] see **Supporting Information, section S9.**

Indeed, assuming that l varies between 8 nm and 12 nm, which is consistent with the size fluctuations reported in Ref. 1, a 50 meV redshift is readily realized between larger NCs and
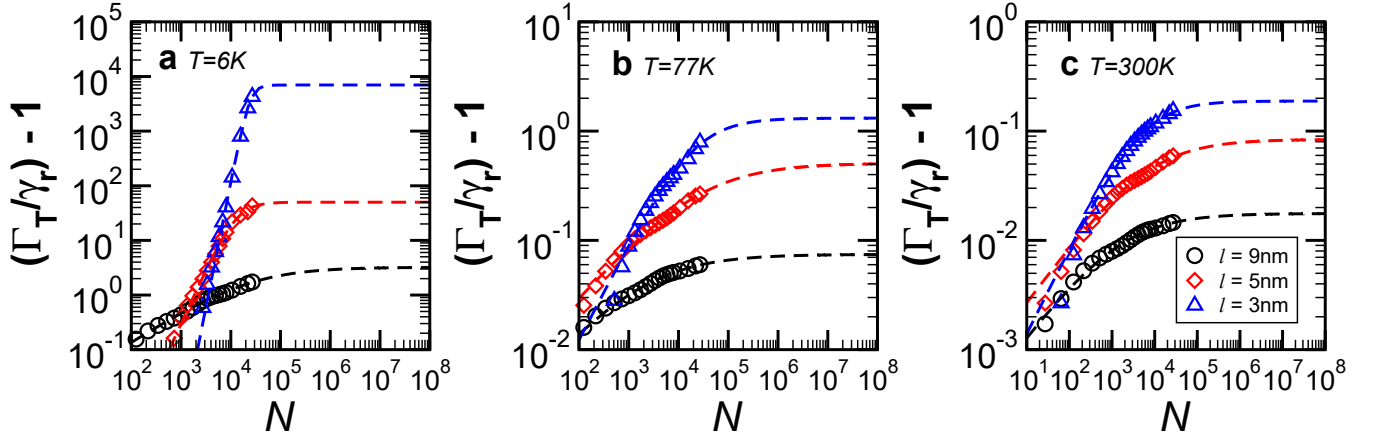
Figure 3: Thermal average of the normalized radiative decay (Eq. (2)) versus N for different temperatures ($T = 6$ K, 77 K, 300 K). In each panel, the temperature is fixed and each color represents a different NC size ($l = 3$ nm, 5 nm, 9 nm, see the legend). Dashed lines are best fits with the function $(\Gamma_T/\gamma_r) - 1 = AN^B/(N^B + N_{sat}^B)$, with fit parameters A, B, N_{sat} (values in **Supporting Information, section S6**). In all panels, the excitation energy is $\hbar\omega_0 = 2.38$ eV and the transition dipole moment is $\mu = 23$ D. The relative dielectric constant of NC superlattice effective medium is $\epsilon_r = 4.8$.

their smaller NC counterparts within a given superlattice's residual size distribution (see details in the **Supporting Information, section S9**). The existence of sub-domains made of larger NCs within a superlattice thus rationalize large redshifts of the SR emission.

How large are the sub-domains? In considering this, we note that thermal decoherence, which occurs on the several picoseconds timescale in CsPbBr$_3$ NCs,[43] cannot be neglected when considering their radiative decay, a process that occurs on the hundred picosecond timescale. This ultimately implies that the aforementioned SR sub-domains must be composed of at least $N = 10^4$ NCs to attain a superradiant decay compatible with experiment, see Fig. 2a.

The existence of SR-active sub-domains also explains the large SR linewidth seen in Ref. 1. Namely, Ref. 1 shows SR to have an inhomogeneous linewidth of tens of meV. This exceeds the estimated static disorder in our model by at least an order of magnitude, see Fig. 2a. The discrepancy, however, can be rationalized by the presence of *multiple* SR-active sub-domains within a given superlattice, which is consistent with the presence of sub-structures in the SR emission band, as noted

in Ref. 1. Namely, provided that these sub-domains are composed of NCs with different average edge lengths, inhomogeneous broadening of the experimetal SR will be seen. In whole, the existence SR sub-domains within a given superlattice, where each sub-domain is composed of large NCs, with an average size that differs from sub-domain to sub-domain, self-consistently rationalizes three observations made in Ref. 1: (1) large 64 ± 6 meV redshifts, (2) large 15 ± 4 meV SR inhomogeneous linewidths and (3) SR emission spectral substructure. For more details, see the discussion in **Supporting Information, section S10**.

Finally, our theoretical framework points to ways of enhancing the SR effect in NC superlattices. Specifically, our model suggests that superlattices made of smaller, tightly packed NCs will exhibit stronger couplings, implying enhanced SR decays and better prospects for realizing high temperature SR.

We demonstrate this by decreasing component NC edge lengths, l, below CsPbBr$_3$'s exciton Bohr diameter of 7 nm.[20,31] In what follows, a NC transition dipole moment of $\mu = 23$ D and a radiative decay rate of $\gamma_r = 2.5$ ns^{-1} is assumed since both parameters are weakly size-dependent in the range of NC

sizes explored.[20,31,44] Near-field dipole coupling strengths, in contrast, increase due to smaller inter-NC separations. This stems from nearest-NC neighbor couplings scaling as $J \approx \mu^2/(l')^3$ (see **Supporting Information, section S2**).

We consider NCs as small as $l = 3$ nm, compatible with the current lower bound for size-controlled $CsPbBr_3$ NCs.[31] In the case of $l = 3$ nm, the estimated coupling between NCs is $J \approx 2.1$ meV. This is 15 times larger than that in the $l = 9$ nm NC superlattice studied in Ref. 1.

Figure 3 shows the dependence of Γ_T with NC superlattice size, for superlattices made of $l = 3$ nm and $l = 5$ nm NCs. The $l = 9$ nm case is included for comparison purposes. Each panel in **Figure 3** considers a different temperature ($T = 6$ K, 77 K, 300 K). It is clear that decreasing l enhances the SR effect at all temperatures. The largest enhancement occurs at $T = 6$ K for $l = 3$ nm.

By assuming enhancement saturation at large N, we estimate Γ_T for realistically large superlattices ($N \sim 10^8$) made of $l = 3, 5, 9$ nm NCs. At $T = 6$ K, we predict $\Gamma_T/\gamma_r \approx 4.2$ for $l = 9$ nm, in excellent agreement with experiment.[1] For $l = 5$ nm and $l = 3$ nm, we find $\Gamma_T/\gamma_r \approx 50$ and $\Gamma_T/\gamma_r \approx 7000$ respectively at $T = 6$ K. The latter $l = 3$ nm enhancement is three orders of magnitude larger than that reported in Ref. 1.

The modeling therefore suggests that small NCs can be used to significantly increase the temperature range where it is possible to observe NC superlattice SR. To illustrate this, **Figure 3b** shows that the expected SR decay rate enhancement for a $l = 3$ nm NC superlattice is $\Gamma_T/\gamma_r \approx 2.3$ at liquid nitrogen temperature ($T = 77$ K). This raises exciting prospects for realizing robust NC superlattice SR at significantly higher temperatures than 6 K in the near future.

Before concluding, it is important to consider the role of static disorder for different NCs sizes. Indeed, band edge transition energies vary with size, especially at small l.[31] This, in turn, implies that small NCs will exhibit energy disorder parameters larger than those of their larger NC counterparts for identical size distributions.

Nevertheless, as shown in **Supporting Information, section S10**, the ratio W/J (where W is the disorder strength and J is the coupling between neighbor NCs) remains almost constant as NC sizes are varied between $l = 3$ nm and $l = 9$ nm. Consequently, since realistic disorder has a minor effect for large NC sizes and for $W/J \approx 15$, we expect a minor effect for small NCs so long as W/J remains of the same order.

In summary, we have developed a theoretical model that explicitly accounts for the effects of thermal decoherence and structural disorder on NC superlattice SR and which rationalizes the SR effect recently observed.[1] Our proposed model also estimates the effects of NC size and temperature on superlattice SR, revealing that superlattices made of smaller, tightly packed NCs will exhibit stronger couplings. Indeed, we predict a SR enhancement of at least three orders of magnitude, using NCs with edge lengths of $l = 3$ nm. This points to the possibility of observing NC superlattice SR at liquid nitrogen temperatures instead of at $T = 6$ K.

We note that our model is generally applicable to other NC assemblies. The only input parameters needed are NC band-edge transition energies, lifetimes, and NC positions within assemblies. Future iterations of the model will account for non-radiative processes in NCs[33] (i.e. non unity emission quantum yields) as well as higher excitation fluences.

Supporting Information Available

Non-Hermitian Hamiltonian for NC superlattices. Point dipole validity. Time-resolved fluorescence at T=0 K without disorder. Geometry dependence of the SR states position. Time-resolved fluorescence with non-zero temperature. Fitting parameters for the saturation function. The saturation assumption. Time-resolved fluorescence at T=0 K with static disorder. Emission redshift. Static disorder and inhomogeneous linewidth.

References

(1) Rainò, G.; Becker, M. A.; Bodnarchuk, M. I.; Mahrt, R. F.; Kovalenko, M. V.; Stöferle, T. Superfluorescence from lead halide perovskite quantum dot superlattices. *Nature* **2018**, *563*, 671–675.

(2) Bonifacio, R.; Lugiato, L. A. Cooperative radiation processes in two-level systems: Superfluorescence. *Phys. Rev. A* **1975**, *11*, 1507–1521.

(3) Dicke, R. H. Coherence in Spontaneous Radiation Processes. *Phys. Rev.* **1954**, *93*, 99–110.

(4) Cong, K.; Zhang, Q.; Wang, Y.; Noe, G. T.; Belyanin, A.; Kono, J. Dicke superradiance in solids [Invited]. *J. Opt. Soc. Am. B* **2016**, *33*, C80–C101.

(5) Araújo, M. O.; Krešić, I.; Kaiser, R.; Guerin, W. Superradiance in a Large and Dilute Cloud of Cold Atoms in the Linear-Optics Regime. *Phys. Rev. Lett.* **2016**, *117*, 073002.

(6) Monshouwer, R.; Abrahamsson, M.; van Mourik, F.; van Grondelle, R. Superradiance and Exciton Delocalization in Bacterial Photosynthetic Light-Harvesting Systems. *The Journal of Physical Chemistry B* **1997**, *101*, 7241–7248.

(7) De Boer, S.; Wiersma, D. A. Dephasing-induced damping of superradiant emission in J-aggregates. *Chemical Physics Letters* **1990**, *165*, 45 – 53.

(8) Fidder, H.; Knoester, J.; Wiersma, D. A. Superradiant emission and optical dephasing in J-aggregates. *Chemical Physics Letters* **1990**, *171*, 529 – 536.

(9) Scheibner, M.; Schmidt, T.; Worschech, L.; Forchel, A.; Bacher, G.; Passow, T.; Hommel, D. Superradiance of quantum dots. *Nature Physics* **2007**, *3*, 106–110.

(10) Brandes, T. Coherent and collective quantum optical effects in mesoscopic systems. *Physics Reports* **2005**, *408*, 315 – 474.

(11) Bradac, C.; Johnsson, M. T.; van Breugel, M.; Baragiola, B. Q.; Martin, R.; Juan, M. L.; Brennen, G. K.; Volz, T. Room-temperature spontaneous superradiance from single diamond nanocrystals. *Nature communications* **2017**, *8*, 1–6.

(12) Higgins, K.; Benjamin, S.; Stace, T.; Milburn, G.; Lovett, B. W.; Gauger, E. Superabsorption of light via quantum engineering. *Nature Communications* **2014**, *5*, 1–7.

(13) Hu, X.; Ritz, T.; Damjanović, A.; Schulten, K. Pigment Organization and Transfer of Electronic Excitation in the Photosynthetic Unit of Purple Bacteria. *the Journal of Physical Chemistry B* **1997**, *101*, 3854–3871.

(14) Strümpfer, J.; Sener, M.; Schulten, K. How quantum coherence assists photosynthetic light-harvesting. *the Journal of Physical Chemistry Letters* **2012**, *3*, 536–542.

(15) Hu, X.; Damjanović, A.; Ritz, T.; Schulten, K. Architecture and mechanism of the light-harvesting apparatus of purple bacteria. *Proceedings of the National Academy of Sciences* **1998**, *95*, 5935–5941.

(16) Şener, M. K.; Olsen, J. D.; Hunter, C. N.; Schulten, K. Atomic-level structural and functional model of a bacterial photosynthetic membrane vesicle. *Proceedings of the National Academy of Sciences* **2007**, *104*, 15723–15728.

(17) Bohnet, J. G.; Chen, Z.; Weiner, J. M.; Meiser, D.; Holland, M. J.; Thompson, J. K. A steady-state superradiant laser with less than one intracavity photon. *Nature* **2012**, *484*, 78–81.

(18) Murray, C. B.; Kagan, C. R.; Bawendi, M. G. Synthesis and Characterization of Monodisperse Nanocrystals and Close-Packed Nanocrystal Assemblies. *Annual Review of Materials Science* **2000**, *30*, 545–610.

(19) Shevchenko, E. V.; Talapin, D. V.; Kotov, N. A.; O'Brien, S.; Murray, C. B. Structural diversity in binary nanoparticle superlattices. *Nature* **2006**, *439*, 55–59.

(20) Becker, M. A.; Vaxenburg, R.; Nedelcu, G.; Sercel, P. C.; Shabaev, A.; Mehl, M. J.; Michopoulos, J. G.; Lambrakos, S. G.; Bernstein, N.; Lyons, J. L., et al. Bright triplet excitons in caesium lead halide perovskites. *Nature* **2018**, *553*, 189–193.

(21) Gross, M.; Haroche, S. Superradiance: An essay on the theory of collective spontaneous emission. *Physics Reports* **1982**, *93*, 301 – 396.

(22) Bellando, L.; Gero, A.; Akkermans, E.; Kaiser, R. Cooperative effects and disorder: A scaling analysis of the spectrum of the effective atomic Hamiltonian. *Phys. Rev. A* **2014**, *90*, 063822.

(23) Guerin, W.; Rouabah, M.; Kaiser, R. Light interacting with atomic ensembles: collective, cooperative and mesoscopic effects. *Journal of Modern Optics* **2017**, *64*, 895–907.

(24) Gullì, M.; Valzelli, A.; Mattiotti, F.; Angeli, M.; Borgonovi, F.; Celardo, G. L. Macroscopic coherence as an emergent property in molecular nanotubes. *New Journal of Physics* **2019**, *21*, 013019.

(25) Grad, J.; Hernandez, G.; Mukamel, S. Radiative decay and energy transfer in molecular aggregates: The role of intermolecular dephasing. *Phys. Rev. A* **1988**, *37*, 3835–3846.

(26) Bettles, R. *Cooperative interactions in lattices of atomic dipoles*; Springer, 2017.

(27) Brennan, M. C.; Toso, S.; Pavlovetc, I. M.; Zhukovskyi, M.; Maras, S.; Kuno, M.; Manna, L.; Baranov, D. Superlattices are greener on the other side: How light transforms self-assembled mixed halide perovskite nanocrystals. *ACS Energy Lett.* **2020**, *5*, 1465–1473.

(28) Vovk, I. A.; Tepliakov, N. V.; Baimuratov, A. S.; Leonov, M. Y.; Baranov, A. V.; Fedorov, A. V.; Rukhlenko, I. D. Excitonic phenomena in perovskite quantum-dot supercrystals. *Phys. Chem. Chem. Phys.* **2018**, *20*, 25023–25030.

(29) Spano, F. C.; Kuklinski, J. R.; Mukamel, S. Temperature-dependent superradiant decay of excitons in small aggregates. *Phys. Rev. Lett.* **1990**, *65*, 211–214.

(30) Meier, T.; Zhao, Y.; Chernyak, V.; Mukamel, S. Polarons, localization, and excitonic coherence in superradiance of biological antenna complexes. *The Journal*

of Chemical Physics **1997**, *107*, 3876–3893.

(31) Brennan, M. C.; Herr, J. E.; Nguyen-Beck, T. S.; Zinna, J.; Draguta, S.; Rouvimov, S.; Parkhill, J.; Kuno, M. Origin of the Size-Dependent Stokes Shift in CsPbBr3 Perovskite Nanocrystals. *Journal of the American Chemical Society* **2017**, *139*, 12201–12208, PMID: 28772067.

(32) Celardo, G. L.; Giusteri, G. G.; Borgonovi, F. Cooperative robustness to static disorder: Superradiance and localization in a nanoscale ring to model light-harvesting systems found in nature. *Phys. Rev. B* **2014**, *90*, 075113.

(33) Frantsuzov, P.; Kuno, M.; Janko, B.; Marcus, R. A. Universal emission intermittency in quantum dots, nanorods and nanowires. *Nature Physics* **2008**, *4*, 519–522.

(34) Frantsuzov, P. A.; Volkán-Kacsó, S.; Jankó, B. Model of Fluorescence Intermittency of Single Colloidal Semiconductor Quantum Dots Using Multiple Recombination Centers. *Phys. Rev. Lett.* **2009**, *103*, 207402.

(35) Frantsuzov, P. A.; Volkán-Kacsó, S.; Jankó, B. Universality of the Fluorescence Intermittency in Nanoscale Systems: Experiment and Theory. *Nano Letters* **2013**, *13*, 402–408.

(36) Baranov, D.; Toso, S.; Imran, M.; Manna, L. Investigation into the Photoluminescence Red Shift in Cesium Lead Bromide Nanocrystal Superlattices. *The Journal of Physical Chemistry Letters* **2019**, *10*, 655–660.

(37) van der Burgt, J. S.; Geuchies, J. J.; van der Meer, B.; Vanrompay, H.; Zanaga, D.; Zhang, Y.; Albrecht, W.; Petukhov, A. V.; Filion, L.; Bals, S.; Swart, I.; Vanmaekelbergh, D. Cuboidal Supraparticles Self-Assembled from Cubic

CsPbBr3 Perovskite Nanocrystals. *The Journal of Physical Chemistry C* **2018**, *122*, 15706–15712.

(38) Nagaoka, Y.; Hills-Kimball, K.; Tan, R.; Li, R.; Wang, Z.; Chen, O. Nanocube Superlattices of Cesium Lead Bromide Perovskites and Pressure-Induced Phase Transformations at Atomic and Mesoscale Levels. *Advanced Materials* **2017**, *29*, 1606666.

(39) Tong, Y.; Yao, E.-P.; Manzi, A.; Bladt, E.; Wang, K.; Döblinger, M.; Bals, S.; Müller-Buschbaum, P.; Urban, A. S.; Polavarapu, L.; Feldmann, J. Spontaneous Self-Assembly of Perovskite Nanocrystals into Electronically Coupled Supercrystals: Toward Filling the Green Gap. *Advanced Materials* **2018**, *30*, 1801117.

(40) Imran, M.; Ijaz, P.; Baranov, D.; Goldoni, L.; Petralanda, U.; Akkerman, Q.; Abdelhady, A. L.; Prato, M.; Bianchini, P.; Infante, I.; Manna, L. Shape-Pure, Nearly Monodispersed CsPbBr3 Nanocubes Prepared Using Secondary Aliphatic Amines. *Nano Letters* **2018**, *18*, 7822–7831.

(41) Kovalenko, M. V.; Bodnarchuk, M. I. Lead halide perovskite nanocrystals: From discovery to self-assembly and applications. *CHIMIA International Journal for Chemistry* **2017**, *71*, 461–470.

(42) Wang, K.-H.; Yang, J.-N.; Ni, Q.-K.; Yao, H.-B.; Yu, S.-H. Metal Halide Perovskite Supercrystals: Gold–Bromide Complex Triggered Assembly of CsPbBr3 Nanocubes. *Langmuir* **2018**, *34*, 595–602.

(43) Brennan, M. C.; Forde, A.; Zhukovskyi, M.; Baublis, A. J.; Morozov, Y. V.; Zhang, S.; Zhang, Z.; Kilin, D. S.; Kuno, M. Universal Size-Dependent Stokes Shifts in Lead Halide Perovskite Nanocrystals. *The Journal of Physical Chemistry Letters* **2020**, *11*, 4937–4944.

10

(44) Kayanuma, Y. Quantum-size effects of interacting electrons and holes in semiconductor microcrystals with spherical shape. *Phys. Rev. B* **1988**, *38*, 9797–9805.

Graphical TOC Entry
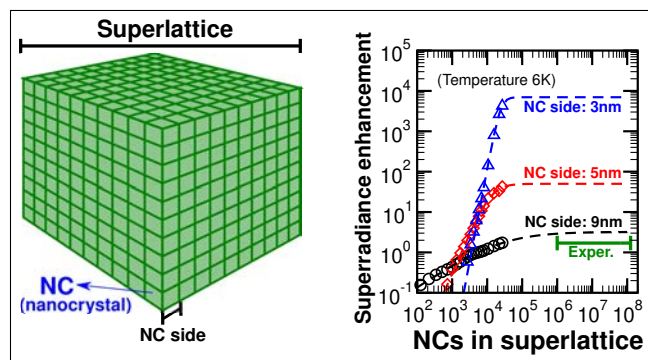
Supporting Information for:

Thermal decoherence of superradiance in lead halide perovskite nanocrystal superlattices

Francesco Mattiotti,*,†,‡,¶ Masaru Kuno,†,§ Fausto Borgonovi,‡,¶ Boldizsár Jankó,† and G. Luca Celardo‖

†*Department of Physics, University of Notre Dame, Notre Dame, IN, USA*

‡*Dipartimento di Matematica e Fisica and Interdisciplinary Laboratories for Advanced Materials Physics, Università Cattolica del Sacro Cuore, Brescia, Italy*

¶*Istituto Nazionale di Fisica Nucleare, Sezione di Pavia, Pavia, Italy*

§*Department of Chemistry and Biochemistry, University of Notre Dame, Notre Dame, IN, USA*

‖*Benemérita Universidad Autónoma de Puebla, Instituto de Física, Puebla, Mexico*

E-mail: fmattiot@nd.edu

Contents

S1   Non-Hermitian Hamiltonian for NC superlattices

Here we describe in detail the radiative hamiltonian $\hat{H}$ (Eq. (1) in the main text), introduced in the main text to rationalize SR-like emission from NC superlattices focusing on the low fluence regime (weak excitation).

In order to build a model able to reproduce the system response to electromagnetic radiation, the features of the NC emitter must be established. The unit element of the superlattice under study is the cubic $CsPbBr_3$ perovskite NC.[1] Because of its cubic symmetry, optical transitions in a $CsPbBr_3$ NC involve three degenerate states (labelled as $\alpha = x, y, z$), each with a transition dipole moment (TDM) equal in magnitude ($\mu_\alpha = \mu$) and perpendicular to the others. A similar situation is found in many atomic systems with isotopic response to electromagnetic excitation.[2,3] Thus we model each NC as a four-level system, with a ground state $|g\rangle$ and three degenerate excited states $|x\rangle$, $|y\rangle$ and $|z\rangle$. Corresponding TDM matrix elements are $\left\langle \alpha \left| \widehat{\vec{\mu}} \right| g \right\rangle = \mu \hat{e}_\alpha$, with $\alpha = x, y, z$ and the Cartesian unit vectors defined as $\hat{e}_\alpha$.

Here we consider an ensemble of cubic NCs and, in particular, focus on a regular cubic superlattice. Since excitons are bound inside each NC, we do not include any overlap inter-

action between different NCs and the only interaction between NCs is mediated by the light field. We thus propose to describe the NC cubic superlattice using the following $3N \times 3N$ radiative Hamitonian,[2,3] which takes the vectorial nature of light into account,

$$\hat{H} = \hbar \left(\omega_0 - i\frac{\gamma_r}{2} \right) \sum_{\alpha \in \{x,y,z\}} \sum_{n=1}^{N} |n, \alpha\rangle \langle n, \alpha| + \sum_{\alpha,\beta \in \{x,y,z\}} \sum_{\substack{m,n=1 \\ (m \neq n)}}^{N} J_{mn}^{\alpha\beta} |m, \alpha\rangle \langle n, \beta| , \qquad \text{(S1)}$$

where $\hbar\omega_0 = 2.38$ eV is the NC transition energy[4] and $\gamma_r = \mu^2 \omega_0^3 \sqrt{\epsilon_r}/(3\pi\epsilon_0 \hbar c^3) = 2.5$ ns^{-1} is the radiative decay rate of a single NC[4] (with $\mu = 23$ D being the single NC TDM, $\epsilon_r = 4.8$ the relative dielectric permittivity at frequency ω_0,[1] ϵ_0 the vacuum permittivity and c the speed of light). In Eq. (S1), $|n, \alpha\rangle$ represents a quantum state where the nth NC is excited in its αth state, while all the other NCs are in their ground state. Interaction terms are non-Hermitian, namely $J_{mn}^{\alpha\beta} = \Omega_{mn}^{\alpha\beta} - \frac{i}{2}\Gamma_{mn}^{\alpha\beta}$ with the real and imaginary parts given, respectively, by

$$\Omega_{mn}^{\alpha\beta} = \frac{\hbar\gamma_r}{2} \left\{ y_0 \left(k_0 r_{mn}\right) \hat{e}_\alpha \cdot \hat{e}_\beta - \frac{y_2 \left(k_0 r_{mn}\right)}{2} \left[\hat{e}_\alpha \cdot \hat{e}_\beta - 3\left(\hat{e}_\alpha \cdot \hat{r}_{mn}\right)\left(\hat{e}_\beta \cdot \hat{r}_{mn}\right)\right] \right\} , \qquad \text{(S2a)}$$

$$\Gamma_{mn}^{\alpha\beta} = \hbar\gamma_r \left\{ j_0 \left(k_0 r_{mn}\right) \hat{e}_\alpha \cdot \hat{e}_\beta - \frac{j_2 \left(k_0 r_{mn}\right)}{2} \left[\hat{e}_\alpha \cdot \hat{e}_\beta - 3\left(\hat{e}_\alpha \cdot \hat{r}_{mn}\right)\left(\hat{e}_\beta \cdot \hat{r}_{mn}\right)\right] \right\} . \qquad \text{(S2b)}$$

In Eq.s (S2), $y_0 (x)$, $y_2 (x)$, $j_0 (x)$, and $j_2 (x)$ are spherical Bessel functions, $k_0 = \omega_0 \sqrt{\epsilon_r}/c$ is the transition wavenumber, ϵ_r is the refractive index at the optical frequency ω_0, r_{mn} is the distance between the mth and nth NC and $\hat{r}_{mn}$ is the unit vector joining them.

Being non-Hermitian, Eq. (S1) has complex eigenvalues $E_k = \hbar \left(\omega_k - i\frac{\Gamma_k}{2} \right)$ that represent the self-energies of eigenstates. Each eigenstate has a finite lifetime $\tau_k = 1/\Gamma_k$ that is inversely proportional to the imaginary part $(-\hbar\Gamma_k/2)$ of the eigenvalue.

Our model specifically applies to the weak excitation regime, where the physics can be described by considering that only one excitation is present in the system. This regime is relevant for the fluorescence measurements in Ref. 4 at low excitation fluence (500 nJ cm^{-2}). Indeed, multiplying the fluence by the area of a superlattice face (~ 1 μm^2) and dividing

by the photon energy (3 eV, see Ref. 4), indicates that, for this fluence value, only $\sim 10^4$ photons are hitting the superlattice. This is a small fraction ($\sim 1\%$) of the number of NCs present in the superlattice, $N \sim 10^6$. The single-excitation approximation is thus appropriate for describing the experiment. The main advantage of the single-excitation approximation is that the Hilbert space scales as N in contrast to the 2^N dimension of the full system. This allowed us to numerically study superlattices containing up to $N = 30^3$ NCs, with an Hamiltonian matrix dimension of $3N \times 3N = 6.561 \times 10^9$. In general, by exploiting the translational invariance of superlattices, even larger sizes could be studied by employing a Bloch-like eigenbasis for the superlattice.[5,6] Nevertheless, we found that the Bloch-like analytical wavefunctions as employed in Ref. 6 for two-dimensional lattices are not the correct choice in our three-dimensional case, since long-range couplings between NCs do not allow to neglect boundary effects (see more details in section S1.1). Note that the effect of the long-range $1/r_{mn}^2$ and $1/r_{mn}$ terms in the Hamiltonian, Eq. (S2), is stronger in three dimensions than in lower dimensions.

S1.1   Discrepancies with the Bloch basis

In the main text we introduced the radiative hamiltonian $\hat{H}$ (Eq. (1)) describing the collective interaction of a CsPbBr$_3$ NC superlattice with the common radiation field. As we discuss in the main text, a similar approach has been introduced by Vovk et al.[6] to model two-dimensional NC superlattices. A common problem to model these systems is that they are made of a very large number of NCs ($N \gtrsim 10^6$), so that it is not possible to deal numerically with the full Hamiltonian matrix, of order N. In Ref. 6 this "size problem" is solved in an elegant way by using the periodicity of the superlattice. As one can see from Eq. (S2), the matrix elements of $\hat{H}$ depend on the positions of the NCs in the superlattice, which are periodic. Therefore, if one neglects the boundary effects, the Hamiltonian becomes translation-invariant on the Bravais lattice $\vec{n}l' = (n_x l', n_y l', n_z l')$ (with $n_{x,y,z}$ integers) and
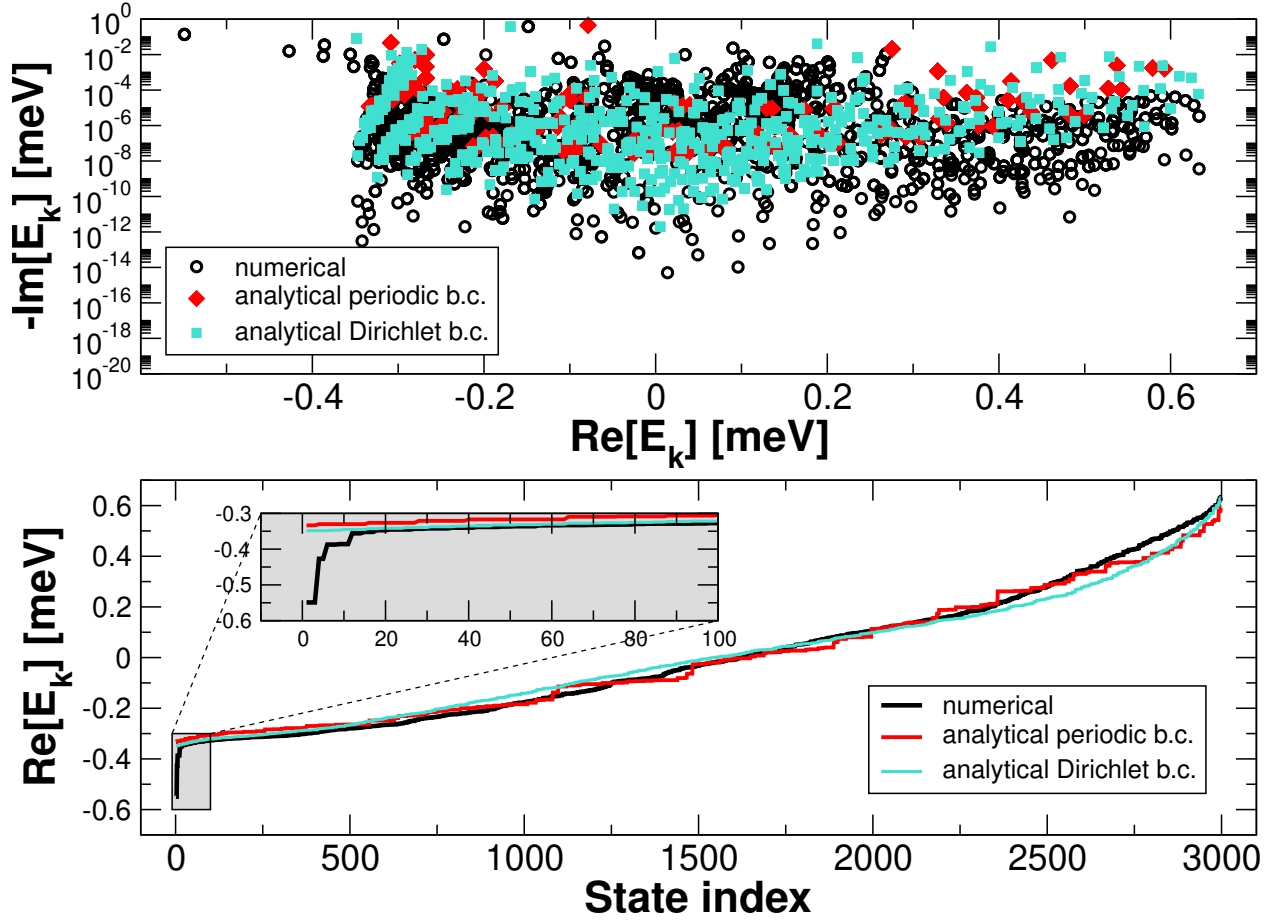
Figure S1: Complex eigenvalues of $\hat{H}$ in the complex plane (upper panel) and their real parts (lower panel), computed from numerical diagonalization and as expectation values $\langle\psi_{\vec{k},u}|\hat{H}|\psi_{\vec{k},u}\rangle$ of the Bloch wavefunctions, Eq. (S3). For the analytical wavefunctions, two different boundary conditions have been considered (see text). Parameters: $\hbar\omega_0 = 2.38$ eV, $\gamma_r = 2.5$ ns^{-1}, $\epsilon_r = 4.8$, $N = 1000$, $l = 9$ nm.

the Bloch Theorem could be applied,[5] implying that the eigenfunctions would have the form

$$\langle \vec{n}, \alpha | \psi_{\vec{k},u} \rangle = \frac{e^{i\vec{k}\cdot\vec{n}}}{\sqrt{N}} c_u^{(\alpha)}(\vec{k}), \qquad \alpha \in \{x, y, z\}, \qquad u = 1, 2, 3. \tag{S3}$$

In Eq. (S3) the vector $\vec{k}$ has N possible values, determined by the boundary conditions, while the $c_u^{(\alpha)}(\vec{k})$ coefficients can be found by diagonalizing a 3×3 matrix for each $\vec{k}$,

$$h_{\alpha\beta}(\vec{k}) = \langle \psi_{\vec{k},\alpha} | \hat{H} | \psi_{\vec{k},\beta} \rangle = \sum_{\vec{m}} \sum_{\vec{n}} \frac{e^{i\vec{k}\cdot(\vec{m}-\vec{n})}}{N} \langle \vec{n}, \alpha | \hat{H} | \vec{m}, \beta \rangle. \tag{S4}$$

The coefficients $c_u^{(\alpha)}(\vec{k})$ in Eq. (S3) are the coefficients that allow to diagonalize $h_{\alpha\beta}(\vec{k})$, and they arise from the coupling between Bloch wavefunctions having the same eigenmode $\vec{k}$ but different polarizations $\alpha, \beta = x, y, z$.

Such approach works very well in presence of nearest-neighbor coupling only, for which boundary effects are negligible, as we verified (data not shown). When boundary effects are negligible, it is convenient to employ periodic boundary conditions to the Hamiltonian, like it has been done in Ref. 6, where the authors use dipolar couplings on a two-dimensional superlattice, so that the couplings are short-range. On the other hand, this approach might not work in our case, that is a cubic superlattice larger than the transition wavelength λ, with long-range radiative couplings scaling as r_{nm}^{-3}, r_{nm}^{-2} and even r_{nm}^{-1} (see Eq. (S2)). In such case, the boundary effects can become important and the choice of the boundary conditions (for example, periodic boundary conditions *vs.* Dirichlet boundary conditions) can lead to different results.

In order to show this, in the following we compare results from exact diagonalization with those obtained using analytical, translational-invariant eigenstates obtained impos- ing different boundary conditions. In Fig. S1 we plot the complex spectrum of $\hat{H}$, that is the real and imaginary parts of the complex eigenvalues $E_k = \hbar \left(\omega_k - i\frac{\Gamma_k}{2} \right)$. We use a cubic superlattice of $N = 1000$ NCs with size $l = 9$ nm. We compare the numerical results obtained from the diagonalization of $\hat{H}$ (black circles) to the expectation values
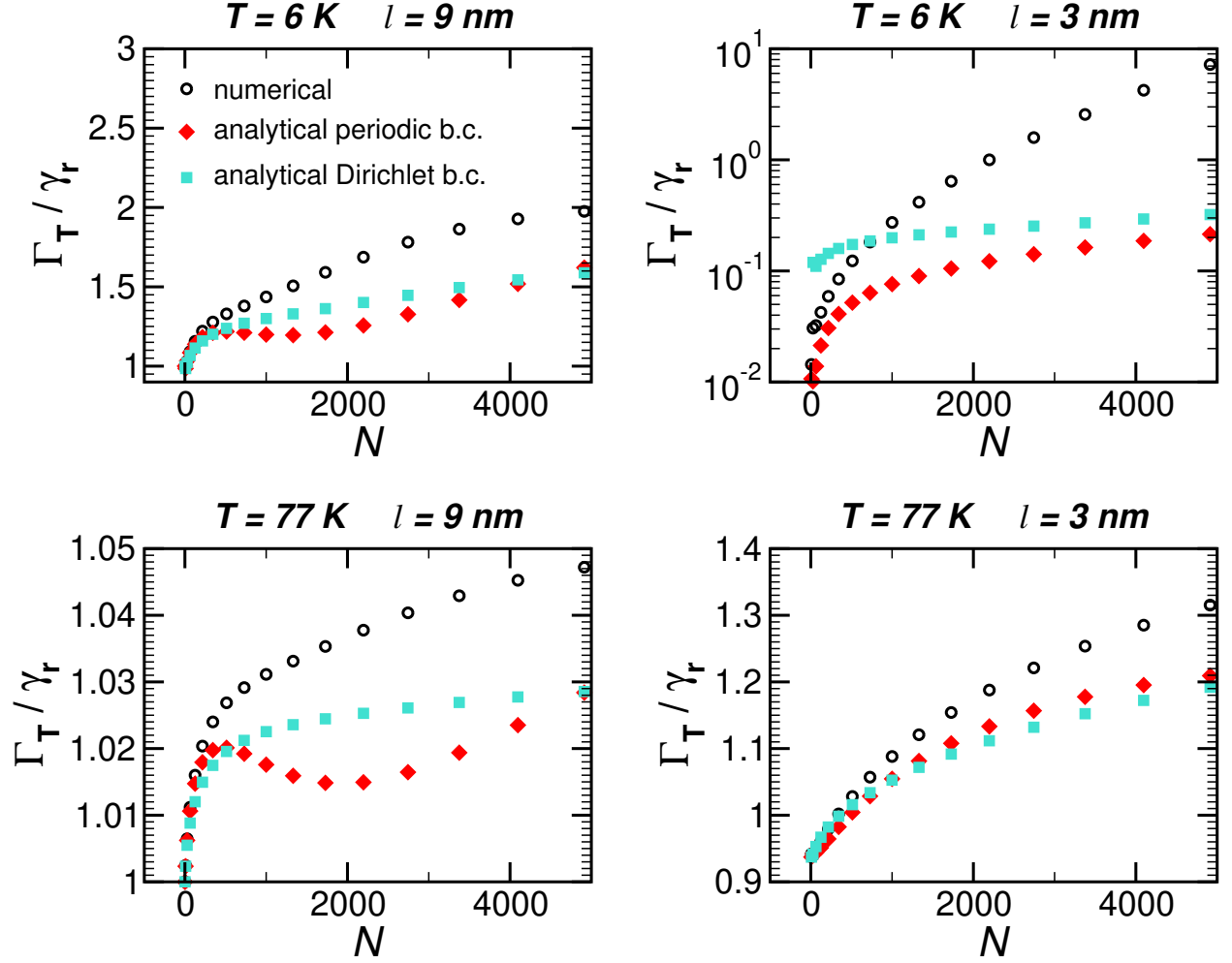
Figure S2: Thermal average of the decay rates (see Eq. (2) in the main text) as a function of the number of NCs in the superlattice. Comparison between numerical eigenvalues and expectation values of $\hat{H}$ over the Bloch wavefunctions, Eq. (S3). Temperature (T) and NC side length (l) indicated over each panel. Parameters: $\hbar\omega_0 = 2.38$ eV, $\gamma_r = 2.5$ ns^{-1}, $\epsilon_r = 4.8$.

$\langle \psi_{\vec{k},u} | \hat{H} | \psi_{\vec{k},u} \rangle$ of the Bloch wavefunctions, using two different boundary conditions (b.c.): periodic b.c. ($e^{i\vec{k}\cdot\vec{n}} = e^{i2\pi\vec{m}_k \cdot \vec{n}/\sqrt[3]{N}}$, with $\vec{m}_k$ vector of integers) and Dirichlet b.c. ($\dfrac{1}{\sqrt{N}} e^{i\vec{k}\cdot\vec{n}} \rightarrow$ $\left(\dfrac{2}{1+\sqrt[3]{N}}\right)^{3/2} \sin\left(\dfrac{\pi m_k^x n_x}{1+\sqrt[3]{N}}\right) \sin\left(\dfrac{\pi m_k^y n_y}{1+\sqrt[3]{N}}\right) \sin\left(\dfrac{\pi m_k^z n_z}{1+\sqrt[3]{N}}\right)$, with $m_k^{x,y,z} = 1, \ldots, \sqrt[3]{N}$, integers). As one can see from the upper panel of Fig. S1, the estimation of the eigenvalues with the Bloch wavefunctions ("analytical") are different from the numerical results. Specifically, there are large differences for the few eigenvalues that have the lowest real part $\text{Re}[E_k]$. These last eigenvalues are particularly important because, once the system reaches thermal equilibrium, most of the population is concentrated at low energy. This discrepancy is also shown in the lower panel of Fig. S1, where the real part of the eigenvalues is plotted against the state index, ordering the eigenvalues according to their real parts. There is a clear discrepancy of about 0.2 meV (that is 40% of $k_B T$ with $T = 6$ K) for the first 10 to 20 eigenvalues (see also the blow-up).

If the discrepancy originates from long-range couplings, then it will increases with N. To check this point, in Fig. S2 we plot the main figure of merit of SR in this work, that is the thermal average of the decay rates (defined in Eq. (2) of the main text), as a function of the system size N for different temperatures ($T = 6$ K, 77 K) and different NC sizes ($l = 3$ nm, 9 nm). As one can see, the results obtained using the analytical Bloch wavefunctions differ from the numerical results and the discrepancy increases with N, indeed. These results suggest that the Bloch basis is not suitable to describe the system at thermal equilibrium.

S2   Point dipole validity

The radiative Hamiltonian introduced in the main text and in section S1 describes the couplings between the TDMs of the NCs treating them as point dipoles. Here we justify such approximation.

In general, the coupling between two excited states localized on different NCs can be described in terms of the Coulomb interaction between the excited state wavefunctions.[7]
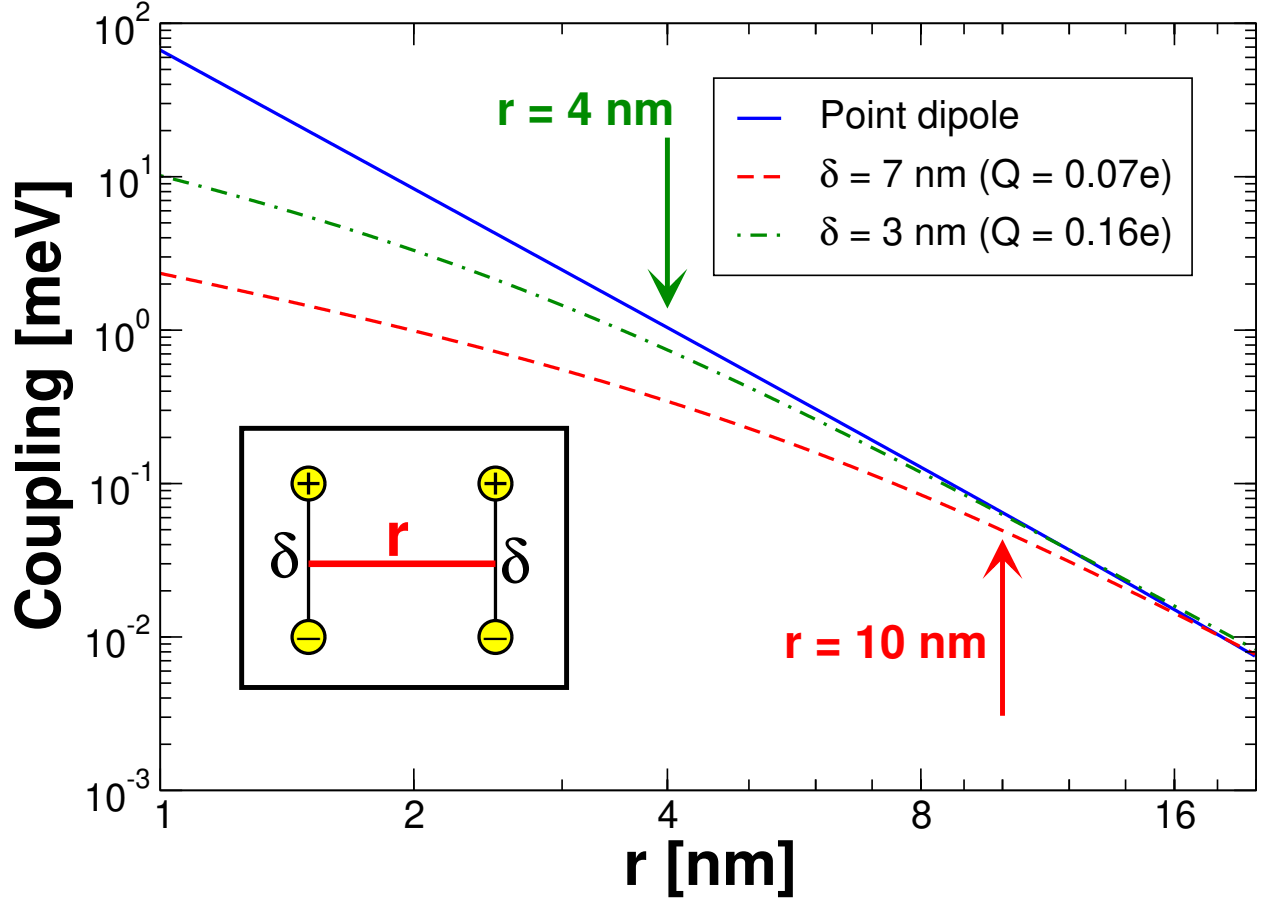
Figure S3: Extended dipole coupling between the TDMs of two NCs (see Eq. (S5)). The relative positions of the partial charges $\pm Q$ are shown pictorially inside the plot. The point dipole coupling is given by Eq. (S6). Parameters: $\mu = 23$ D, $\epsilon_r = 4.8$.

In most practical cases, the Coulomb coupling between two extended wavefunctions can be mapped to the so-called "extended dipole coupling",[7] that is the Coulomb interaction between four effective charges (two for each wavefunction, with opposite sign). The extended dipole coupling has the form

$$V_{mn} = \frac{Q^2}{4\pi\epsilon_0\epsilon_r} \left(\frac{1}{r_{++}} + \frac{1}{r_{--}} - \frac{1}{r_{+-}} - \frac{1}{r_{-+}} \right) \tag{S5}$$

where $r_{++} = |\vec{r}_{m+} - \vec{r}_{n+}|$, $r_{--} = |\vec{r}_{m-} - \vec{r}_{n-}|$, $r_{+-} = |\vec{r}_{m+} - \vec{r}_{n-}|$ and $r_{-+} = |\vec{r}_{m-} - \vec{r}_{n+}|$. The position of the "$\pm$" charge in the nth dipole is $\vec{r}_{n\pm} = \vec{r}_n \pm (\delta/2)\hat{e}_n$, where $\hat{e}_n$ is the unit vector of the nth dipole, δ is the effective charge displacement in the dipole and Q is the partial charge, that is an effective point charge used to describe the coupling. These parameters must satisfy the constraint $\mu = Q\delta$, where μ is the magnitude of the TDM.

If the charge displacement is small with respect to the distance between the dipoles, i.e. $\delta \ll |\vec{r}_m - \vec{r}_n|$, the extended dipole coupling is approximated by the near-field point-dipole coupling, that is

$$V_{mn} \approx \frac{\mu^2 \left[\hat{e}_m \cdot \hat{e}_n - 3 \left(\hat{e}_m \cdot \hat{r}_{mn} \right) \left(\hat{e}_n \cdot \hat{r}_{mn} \right) \right]}{4\pi\epsilon_0\epsilon_r |\vec{r}_m - \vec{r}_n|^3} \tag{S6}$$

where $\hat{r}_{mn} = (\vec{r}_m - \vec{r}_n)/|\vec{r}_m - \vec{r}_n|$.

In the case of NCs, the excitons are bound inside the NC volume due to quantum confinement.[8] Therefore, the charge displacement is bounded by l, that is the edge length of the NC, and by the exciton Bohr diameter $2a_B$ (where a_B is the exciton Bohr radius).

In Fig. S3 we plot the extended dipole coupling, see Eq. (S5), for a pair of TDMs against their center-to-center distance r, comparing it to the point dipole coupling, Eq. (S6). We employ the typical parameters of $CsPbBr_3$ NCs, that is the magnitude $\mu = 23$ D and dielectric constant $\epsilon_r = 4.8$, and we consider a pair of TDMs oriented perpendicularly to the joining vector (see the pictorial representation in the box inside Fig. S3), but a similar result can be obtained with different orientations. For the charge displacement δ we consider two typical situations: $\delta = 2a_B = 7$ nm, that is the maximal charge displacement for large NCs,

10

and $\delta = 3$ nm, corresponding to the maximal charge displacement for the smallest NC side length that we considered in the main text. As one can see from Fig. S3, the extended dipole coupling is well approximated by the point dipole if r is larger than some value, proportional to δ. For a fixed value of r, the agreement with the point dipole approximation is better for smaller charge displacement δ. In particular, we checked the difference in the couplings between nearest neighbour NCs in two cases: (a) $\delta = 7$ nm and $r = 10$ nm, that is NCs with $l = 9$ nm (red arrow), and (b) $\delta = 3$ nm and $r = 4$ nm, corresponding to NCs with $l = 3$ nm (green arrow). In both cases the point dipole coupling overestimates the extended dipole coupling by $\sim 30\%$.

We conclude that the point dipole coupling captures correctly the order of magnitude of the nearest neighbor couplings, assuming the maximal charge displacement in typical cases. The accuracy of the point dipole approximation improves on decreasing the charge displacement, and since we obtain a discrepancy of $\sim 30\%$ for the maximal δ, the actual charge displacement in these NCs is likely smaller than what we considered, implying a better accuracy.

S3   Time-resolved fluorescence at T = 0 K without disorder

Here we proceed to use the Hamiltonian $\hat{H}$, see Eq. (1) in the main text, to compute the time evolution of an excitation initially absorbed by the superlattice.

At $T = 0$ K, the dynamics of the system are governed by the time-dependent Schrödinger equation

$$i\hbar \frac{d}{dt} |\psi(t)\rangle = \hat{H} |\psi(t)\rangle. \tag{S7}$$

The non-Hermiticity of $\hat{H}$ results in a non-unitary time evolution of the excitation in the

superlattice.[9] As an example, if the initial state is an eigenstate $|\psi(0)\rangle = |k\rangle$ of $\hat{H}$ satisfying

$$\hat{H}|k\rangle = \hbar\left(\omega_k - \frac{i}{2}\Gamma_k\right)|k\rangle,\tag{S8}$$

then the total excitation of the system at time t, as quantified by the squared norm of the time-evolved state $|\psi(t)\rangle$, decays exponentially,

$$\langle\psi(t)|\psi(t)\rangle = e^{-\Gamma_k t}.\tag{S9}$$

The decay time $\tau_k = 1/\Gamma_k$ is inversely proportional to the imaginary part $(-\hbar\Gamma_k/2)$ of the eigenvalue.

Here we show the signature of SR in the dynamics, studying the time dependence of the emitted intensity using a master equation approach. As an initial state, we consider an incoherent statistical average of all NC levels. This corresponds to an excited state created by the absorption of an off-resonant photon.[10,11] The state is described by the density operator

$$\hat{\rho}(0) = \frac{1}{3N}\sum_{\alpha\in\{x,y,z\}}\sum_{n=1}^{N}|n,\alpha\rangle\langle n,\alpha|,\tag{S10}$$

which evolves under the generalized Liouville-Von Neumann master equation

$$i\hbar\frac{d}{dt}\hat{\rho}(t) = \hat{H}\hat{\rho}(t) - \hat{\rho}(t)\hat{H}^{\dagger}.\tag{S11}$$

Eq. (S11) is formally equivalent to the Schrödinger equation (Eq. (S7)). Its formal solution is

$$\hat{\rho}(t) = e^{-i\hat{H}t/\hbar}\hat{\rho}(0)e^{i\hat{H}^{\dagger}t/\hbar} = \frac{1}{3N}\sum_{\alpha\in\{x,y,z\}}\sum_{n=1}^{N}e^{-i\hat{H}t/\hbar}|n,\alpha\rangle\langle n,\alpha|e^{i\hat{H}^{\dagger}t/\hbar}\tag{S12}$$

from which we obtain the emitted intensity by taking the product of the excitation energy

12

by the negative derivative of the excitation's survival probability

$$I\left(t\right) = -\hbar\omega_0\frac{d}{dt}\text{tr}\left[\hat{\rho}\left(t\right)\right] = -\frac{\hbar\omega_0}{3N}\frac{d}{dt}\sum_{\alpha,\beta\in\{x,y,z\}}\sum_{m,n=1}^{N}\left|\langle m,\beta|\,e^{-i\hat{H}t/\hbar}\,|n,\alpha\rangle\right|^2$$

$$= -\frac{\hbar\omega_0}{3N}\frac{d}{dt}\sum_{\alpha\in\{x,y,z\}}\sum_{n=1}^{N}P_{n,\alpha}\left(t\right). \tag{S13}$$

In Eq. (S13) $\text{tr}\left[\hat{\rho}\left(t\right)\right]$ is the trace of the density operator and we have defined the probability to find the excitation in the superlattice at time t starting from the NC state $|n,\alpha\rangle$ as

$$P_{n,\alpha}\left(t\right) = \sum_{\beta\in\{x,y,z\}}\sum_{m=1}^{N}\left|\langle m,\beta|\,e^{-i\hat{H}t/\hbar}\,|n,\alpha\rangle\right|^2. \tag{S14}$$

As a point of comparison, note that the survival probability of a single NC's excited state is $P_0(t) = e^{-\gamma_r t}$ which, in turn, yields an exponential decay of the emission intensity $I_0\left(t\right) = \hbar\omega_0\gamma_r e^{-\gamma_r t}$.

The result from Eq. (S13) allows us to numerically compute the emitted intensity versus time by knowing the spectrum of $\hat{H}$. For the NCs considered here, $\lambda = \frac{\lambda_0}{n_r} = 238$ nm where $\lambda_0 = 521$ nm is the band-edge transition wavelength in vacuum and $n_r = \sqrt{\epsilon_r} = 2.19$ is the refractive index of bulk $CsPbBr_3$ at the optical frequency ω_0.[1] The other model parameters are a NC side length of 9 nm and a NC radiative lifetime of $1/\gamma_r = 400$ ps. Note that the radiative lifetime we chose in our model for the single NC is in good agreement with the experimental results for the intensity emission from single NC, compare blue line and blue symbols in Fig. S4. The blue circles are the experimental (6 K) excited state emission decay of an ensemble of non-interacting NCs, characterized by a short timescale, near exponential decay followed by a longer-lived component. The former is attributed to radiative decay while the latter is thought to stem from delayed trap-related emission.

Using this approach, we compute the intensity versus time by applying Eq. (S13) to a $10 \times 10 \times 10$ NC superlattice. Fig. S4 shows the results of our simulations for the time evolution of the emitted intensity (solid red line), compared with the experimental intensity
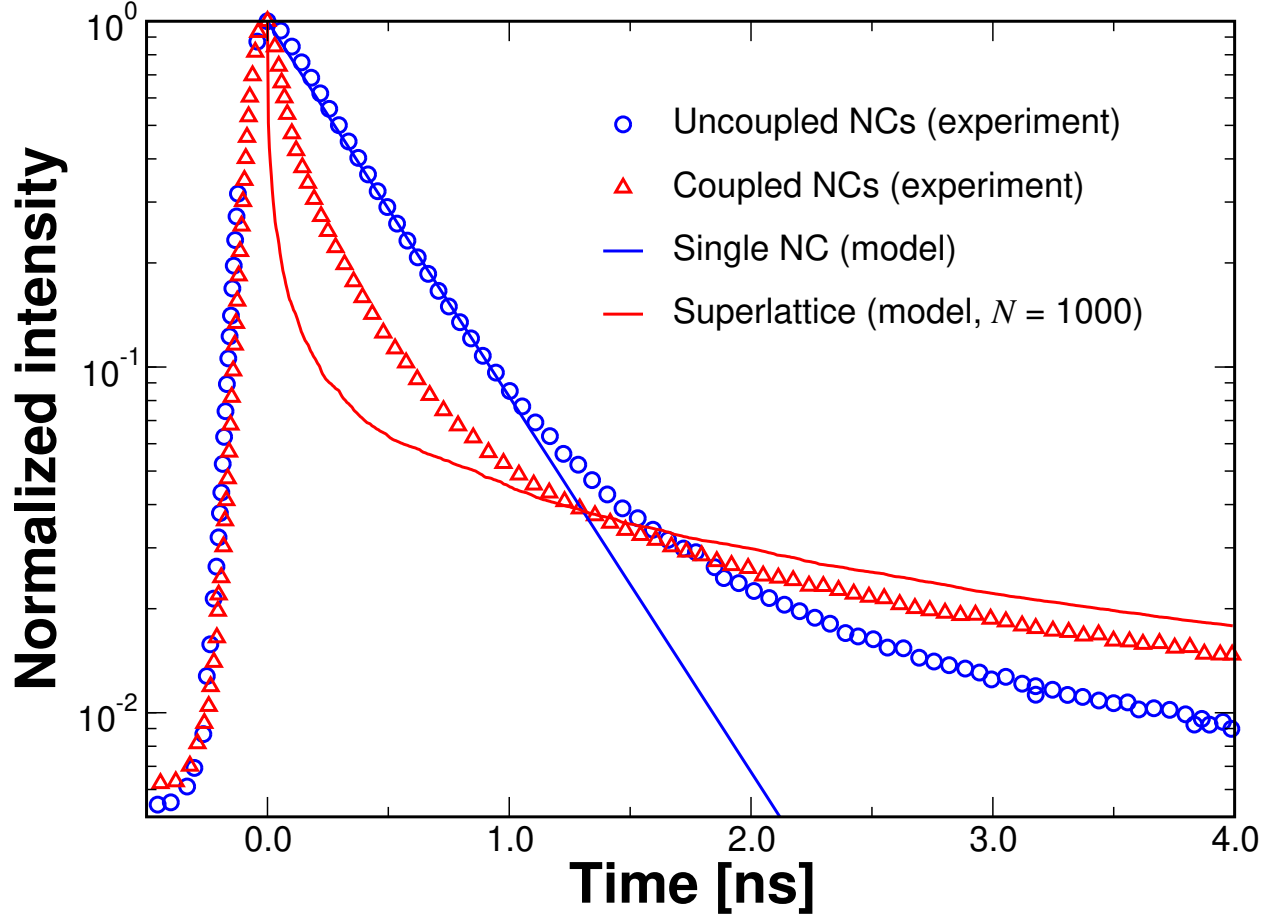
Figure S4: Theoretical emission intensity (see Eq. (S13)) *vs.* time for a single NC (blue line) and for a superlattice of coupled NCs (red line). Parameters: $\hbar\omega_0 = 2.38$ eV, $\gamma_r = 2.5$ ns^{-1}, $\epsilon_r = 4.8$, $l = 9$ nm. Experimental time-resolved photoluminescence (TR-PL) decays from Ref. 4 shown by open symbols of the same color. Time=0 in PL experiments is determined as when the excitation pulse turns off.

decays in time from Ref. 4 (red triangles). Of note is the faster initial decay observed experimentally for the case of coupled NCs (red triangles), which is approximately three times faster than the decay for the uncoupled NC measurements (blue circles). While our results for $T = 0$ K and $N = 10^3$ NCs in the superlattice (red curve) qualitatively reproduce the increased recombination rate seen experimentally, they overestimate the initial, short time experimental rate by nearly four orders of magnitude, according with what is observed in Fig. 1b of the main text. As we discuss in the main text, a number of possible reasons exists for this discrepancy. They center on the absence of thermalization and structural disorder in our model. In section S8, we refine the model in a way that incorporates static disorder.

S4 Geometry dependence of the SR states position

In Fig. 1a of the main text the complex spectrum of the radiative Hamiltonian $\hat{H}$ (see Eq. (1) in the main text) is shown for a cubic superlattice. In this case the most SR state (circled in green in Fig. 1a) lies in the middle of the energy spectrum. In general, the exact energy of the most SR state in a system is exquisitely sensitive to the exact geometrical arrangement of emitting dipoles.

When the dipole is perpendicular to the joining vector between the emitters, the position of the most SR state is blueshifted with respect to the single emitter, as is typical of H-aggregates.[12] On the other side, when the dipoles are parallel to the joining vector, one has a redshifted SR state, as is typical of J-aggregates.[12] The isotropic nature of the NCs considered here implies that, for each NC, three dipole directions have to be considered, each coupled to all the other NC dipole directions. Thus, there are both dipoles parallel to the joining vector between the NCs (i.e. $|\hat{e}_\alpha \cdot \hat{r}_{mn}| = 1$ in Eq. (1) of the main text), giving a redshift contribution, and also dipoles perpendicular to the joining vector (i.e. $|\hat{e}_\alpha \cdot \hat{r}_{mn}| = 0$), giving a blueshift contribution. Due to this mixture of redshift and blueshift contributions,

it is not surprising that the most SR state is close to the middle of the spectrum.
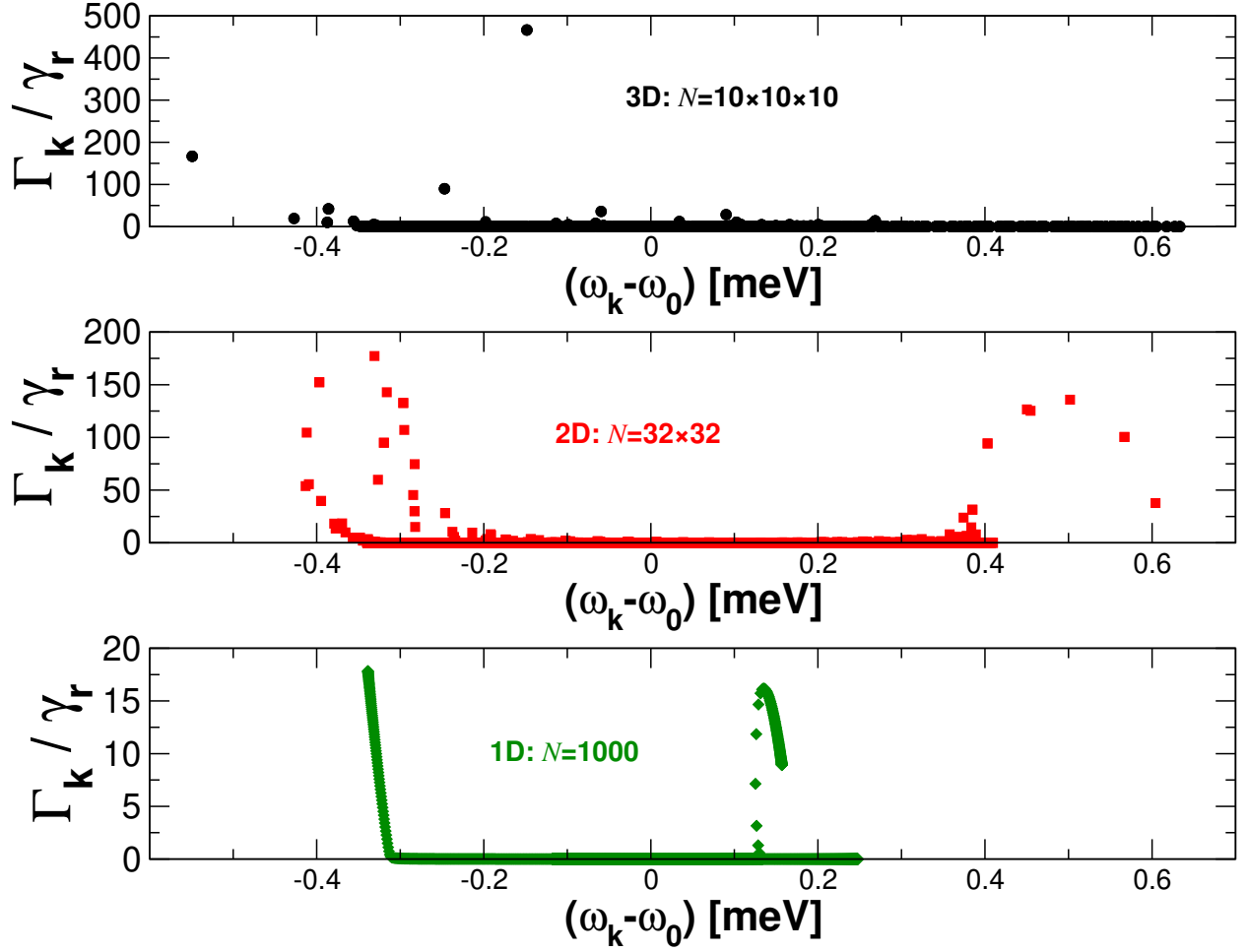

Figure S5: Complex eigenvalues of $\hat{H}$ in the complex plane for a superlattice of $N \approx 1000$ NCs. Each panel correspond to a different arrangement of the NCs in the superlattice: a perfect cube (upper panel), a two-dimensional square 'slab' (middle panel) and a chain (lower panel). Parameters: $\hbar\omega_0 = 2.38$ eV, $\gamma_r = 2.5$ ns^{-1}, $\epsilon_r = 4.8$, $l = 9$ nm.

The position of the most SR states is highly dependent on geometry. Indeed our preliminar results for a 1D and 2D superlattice (see Fig. S5) show that the most SR states are concentrated at the spectrum edges. This peculiar dependence on geometry is strongly determined by the presence of three degenerate TDMs for each NC, which implies a complicated mixture of redshift and blueshift contributions as explained above.

Finally, we note that identifying the energy of the highest SR state with respect to the thermal energy $k_B T$ in an isotropic three-dimensional lattice is not trivial, as the energy

of the highest SR state depends on different parameters. These include lattice geometry[13] and the coupling between distant NCs, which depends on the ratio of the superlattice edge length (L) to the emission wavelength (λ) in the superlattice, i.e. L/λ (see discussions in section S1.1 and section S7).

S5   Time-resolved fluorescence with non-zero temperature

In order to estimate the effect of thermal decoherence on the decay rate of the NC superlattice, one can use the following common theoretical argument.[14] Let us consider the time evolution of an excitation initially present in the system, which is coupled to a thermal bath. Let us write a Pauli master equation[15] for the population $P_k(t)$ of each kth eigenstate,

$$\frac{dP_k(t)}{dt} = -\Gamma_k P_k(t) + \sum_{j=1}^{3N} [R_{kj} P_j(t) - R_{jk} P_k(t)] \ , \tag{S15}$$

where R_{kj} are the thermalization rates between the eigenstates obeying the detailed balance relation $R_{kj} = R_{jk} e^{-\hbar(\omega_k - \omega_j)/(k_B T)}$, while Γ_k is the radiative decay rate of the $k-$th eigenstate. In typical situations, the radiative decay rates Γ_k are much smaller than the thermalization rates, namely $\Gamma_k \ll R_{kj}$. Since thermalization time is smaller than fluorescence time, one can describe time-resolved fluorescence assuming that the system is always at thermal equilibrium, i.e. the populations of the eigenstates follow $P_k(t) \approx P(t) e^{-\hbar\omega_k/k_B T}/Z$ at all times, where $P(t) = \sum_k P_k(t)$ is the excitation survival probability in the system and $Z = \sum_k e^{-\hbar\omega_k/(k_B T)}$ is the partition function. Under this ansatz, the second term in the right hand side of Eq. (S15) is zero. Moreover, summing both sides of Eq. (S15) over k, we have

$$\frac{dP(t)}{dt} = -\Gamma_T P(t) \ , \tag{S16}$$

17

where we have defined the thermal rate

$$\Gamma_T = \frac{1}{Z} \sum_{k=1}^{3N} \Gamma_k e^{-\hbar\omega_k/(k_B T)} \ . \tag{S17}$$

Eq. (S16) has solution $P(t) = \exp(-\Gamma_T t)$. The emitted intensity at time t is related to the survival probability by $I(t) = -\hbar\omega_0 \frac{dP(t)}{dt}$, so that we obtain $I(t) = \hbar\omega_0 \Gamma_T \exp(-\Gamma_T t)$. When $k_B T$ is much larger than the spectral width spanned by the real components $\hbar\omega_k$, thermal mixing of eigenstates suppresses coherence in the system, the thermal average is approximately the arithmetic average $\Gamma_T \simeq \gamma_r$ and the SR is effectively destroyed. This can be easily proven by letting $k_B T$ tend to infinity in Eq. (S17) and using the decay rate sum rule $\sum_{k=1}^{3N} \Gamma_k = 3N\gamma_r$, which stems from the conservation of total oscillator strength.[16] In the superlattice under consideration, the thermal energy at 6 K ($k_B T = 0.5$ meV, grayed area in Fig. 1a in the main text) is smaller but comparable to the spectral width.

In deriving Eq. (S17) we implicitly assume that thermal relaxation, which is typically on the picosecond timescale,[17] dominates all other relaxation processes in the material. Since at realistic sizes the maximal superradiant decay $\Gamma_{SR}^{-1} \approx \tau_r/10^4 \approx 40$ fs could be faster than other disorder-induced relaxation processes, this implies that our thermal decay rate constitutes a lower bound for the SR decay. Indeed, decay rates faster than thermal relaxation would result in an even faster initial SR decay.

S6 Fitting parameters for the saturation function

In the main text (see Fig. 2a and Fig. 3) we introduce the fitting function

$$\frac{\Gamma_T}{\gamma_r} - 1 = \frac{A N^B}{N^B + N_{sat}^B} \ , \tag{S18}$$

where A, B, N_{sat} are fitting parameters. Here, in Table 1, we report the values of the fit parameters for all the data sets shown in the main text (Fig. 2a and Fig. 3).

Table 1: Fit parameters for the data in Fig. 2a and Fig. 3 of the main text, using Eq. (S18).

Temperature	NC sidelength (disorder)	A	B	N_{sat}
$T = 6$ K	$l = 9$ nm ($W = 0$)	3.22	0.58	21978
	$l = 9$ nm ($W = 2$ meV)	2.28	0.47	36954
	$l = 9$ nm ($W = 3$ meV)	0.96	0.53	5061
	$l = 9$ nm ($W = 10$ meV)	0.33	0.56	1424
	$l = 5$ nm	50	1.99	13075
	$l = 3$ nm	6977	4.58	24440
$T = 77$ K	$l = 9$ nm	0.0745	0.51	1816
	$l = 5$ nm	0.508	0.51	23290
	$l = 3$ nm	1.31	0.89	19280
$T = 300$ K	$l = 9$ nm	0.0176	0.52	1384
	$l = 5$ nm	0.084	0.53	6194
	$l = 3$ nm	0.188	0.79	5014

S7 The saturation assumption

In the main text we assume that the thermal SR rate Γ_T saturates to a N-independent value, when the NC density N/L^3 is kept fixed. To justify this assumption, let us analyze the thermal decay rate Γ_T (see Eq. (2) in the main text) considering, for the moment, the following crude approximation for the Boltzmann occupation numbers,

$$\frac{e^{-\hbar\omega_k/(k_BT)}}{Z} \approx \begin{cases} 1/N_T & \text{for } \hbar(\omega_k - \omega_1) \leq k_BT \\ 0 & \text{elsewhere} \end{cases}, \tag{S19}$$

where N_T is the number of superlattice eigenstates having energy $\hbar(\omega_k - \omega_1) \leq k_BT$, with $\hbar\omega_1$ being the minimal energy in the spectrum. Under the approximation in Eq. (S19), we can approximate Eq. (2) of the main text as

$$\frac{\Gamma_T}{\gamma_r} \approx \frac{1}{N_T} \sum_{\hbar(\omega_k-\omega_1)\leq k_BT} \frac{\Gamma_k}{\gamma_r}. \tag{S20}$$

Moreover, as one can see from Fig. 1a in the main text, the sum of the Γ_k/γ_r for the states at low energy ($\hbar(\omega_k - \omega_1) \leq k_BT$) results in a large fraction of the total of the radiative

decay rates in the system (which is $\sum_k \Gamma_k/\gamma_r = 3N$). Since the total of the Γ_k grows as the number N of NCs, we assume that also the sum in Eq. (S20) grows as $\sim N$. We can estimate the number of states N_T at low energy assuming a constant density of states in the spectrum. This rough approximation is justified since $k_B T$ is comparable to the spectral width $\hbar\Delta\omega$. Therefore, $N_T \approx 3N\frac{k_B T}{\hbar\Delta\omega}$, that is the total number $3N$ of eigenstates multiplied by the fraction of $k_B T$ over the spectral width. Under these approximations, we predict that Γ_T/γ_r scales as

$$\frac{\Gamma_T}{\gamma_r} \sim \frac{\hbar\Delta\omega}{k_B T} \ . \tag{S21}$$

Therefore, we proceed to estimate how $\Delta\omega$ scales with the superlattice parameters N and L. This will also allow us to estimate how Γ_T/γ_r scales with those parameters, thanks to Eq. (S21).

Let us consider two limiting cases: (a) $L/\lambda \ll 1$ and (b) $L/\lambda \gg 1$. In case (a) it is known[13] that the coupling is dominated by dipole-dipole near-field terms. Since the dipole-dipole coupling decays as $1/r_{mn}^3$, the interaction is short-range. In such case, the spectral width scales proportionally to the nearest-neighbor coupling, namely $\hbar\Delta\omega \sim \mu^2/(l')^3 \sim N/L^3$, since the center-to-center distance is $l' = L/N^{1/3}$. Thus, thanks to Eq. (S21), we estimate $\Gamma_T/\gamma_r \sim N/L^3$ for $L/\lambda \ll 1$. This estimate is valid in the case of CsPbBr$_3$ for realistic superlattice edge length, even if $L \approx 5\lambda$. In fact (see Fig. S6) $[(\Gamma_T/\gamma_r) - 1]$ is proportional to the density N/L^3 in a broad range of parameters and, specifically, in the experimental case where $l = 9$ nm (see vertical line in Fig. S6). Therefore, $[(\Gamma_T/\gamma_r) - 1]$ depends only on the density and it must saturate to a N-independent value when N is increased keeping the density fixed.

Nevertheless, this scaling is not true in general. For comparison, let us consider the opposite case (b), where the $1/r_{mn}^2$ and $1/r_{mn}$ terms in the hamiltonian (Eq. (S2)) are much more relevant and one can expect a different scaling of the spectral width. The case of $L > \lambda$ has been studied in literature,[2] for densities $N/(L/\lambda)^3 < 200$, much smaller tnan the superlattices analyzed in this work where $N/(L/\lambda)^3 > 10^4$. It has been found that
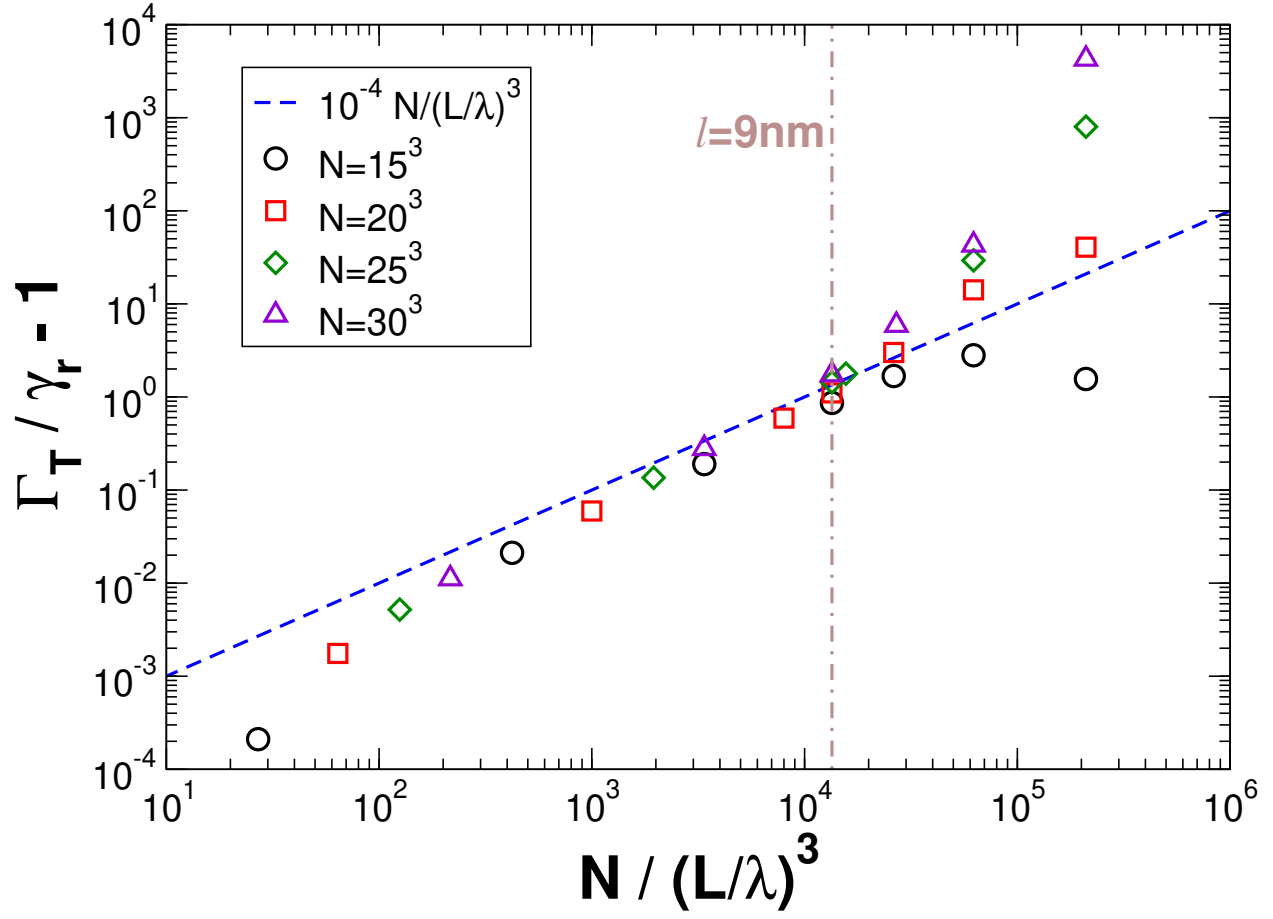
Figure S6: Thermal SR decay (see Eq. (2) in the main text) as a function of the NC density in the superlattice, at temperature $T = 6$ K. Parameters: $\hbar\omega_0 = 2.38$ eV, $\gamma_r = 2.5$ ns^{-1}, $\epsilon_r = 4.8$.
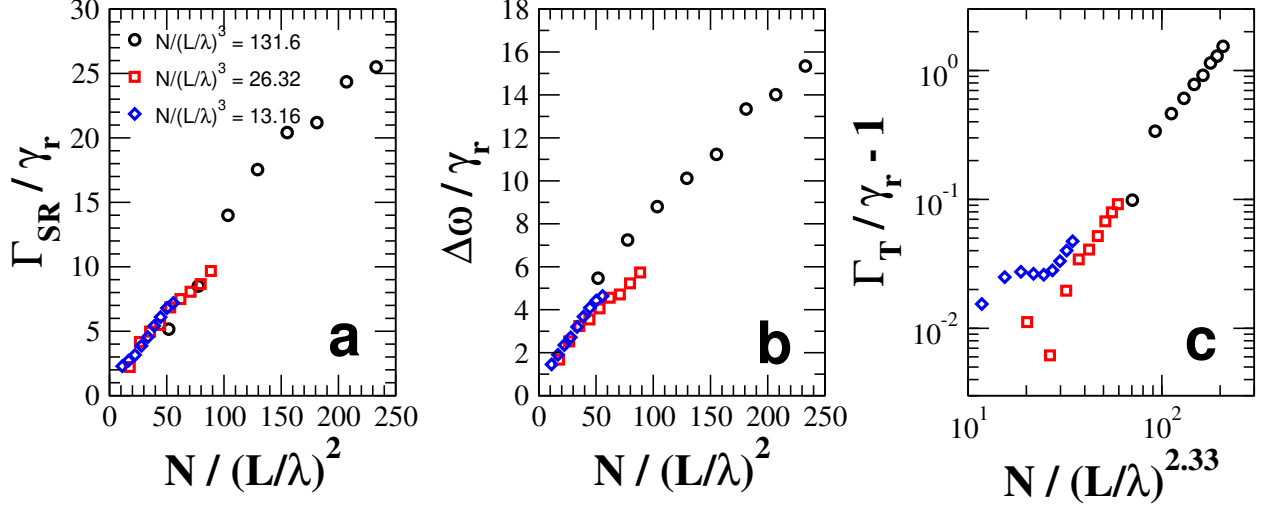
Figure S7: **a** Maximal decay rate for the superlattice eigenstates, **b** energy range spanned by the eigenvalues and **c** thermal decay rate ($T = 60$ mK) for superlattices (see Eq. (2) in the main text) at low density of NCs (see legend in panel (a)). Parameters: $\hbar\omega_0 = 2.38$ eV, $\gamma_r = 2.5$ ns^{-1}, $\epsilon_r = 4.8$.

the spectral widths in the complex plane (that is, the maximal imaginary part Γ_{SR} and the energy width $\hbar\Delta\omega$) scale proportionally to $N/(L/\lambda)^2$. Even if the atomic clouds in Ref. 2 are completely disordered, while superlattices are ordered, the conclusions by Bellando et al.[2] are valid also for regular superlattices having the same low densities used for atomic clouds. Specifically, in Fig. S7a-b we find that both Γ_{SR} and $\Delta\omega$ scale proportionally to $N/(L/\lambda)^2$ for large volumes and small densities. Therefore, using Eq. (S21), we predict $\Gamma_T/\gamma_r \sim N/(L/\lambda)^2$ in this regime. Then, we proceed to check such prediction for Γ_T/γ_r using the correct definition from Eq. (2) in the main text, and for $T = 60$ mK, so that $(k_B T)/(\hbar\Delta\omega) \approx 1/3$ like in the superlattice considered in this work. The results are shown in in Fig. S7c where we plot $\Gamma_T/\gamma_r - 1$ for the same data shown in Fig. S7a-b. Optimizing the linear correlation, we find (see Fig. S7c) that the optimal scaling is established between $\Gamma_T/\gamma_r - 1$ and $N/(L/\lambda)^{2.33}$. Note that 2.33 is close to our rough prediction (2) and smaller than 3 (obtained above for the realistic, high-density case).

S8 Time-resolved fluorescence at T = 0 K with static disorder

To further refine our model, we account for energetic heterogeneities as static disorder, parametrized by additional site-energy fluctuations in the Hamiltonian

$$\hat{H} \to \hat{H} + \sum_{\alpha \in \{x,y,z\}} \sum_{n=1}^{N} \delta_{n,\alpha} \left| n, \alpha \right\rangle \left\langle n, \alpha \right| \tag{S22}$$

uniformly distributed within the range $-\frac{W}{2} \leq \delta_{n,\alpha} \leq \frac{W}{2}$. Static disorder is known to destroy SR.[18] Since our simulations in absence of disorder clearly overestimate SR (see Fig. S4), we may expect that the addition of static disorder would quench SR and therefore improve the accuracy of our model.

In Fig. S8 we plot the decay of the emitted intensity from a superlattice. The experiment has been conducted for $N \sim 10^6$, while we use $N = 1000$ in the simulations (continuous lines). The black line is the same as the model results from Fig. S4 in absence of disorder, while the blue and green lines have been obtained using different values of static disorder. Since the nearest-neighbor coupling is $J = 0.14$ meV, we consider a disorder value comparable to the coupling ($W = 0.1$ meV) and another much larger than J ($W = 1$ meV). In both cases, the agreement between the model and the experiment is not better than the case at $W = 0$: the initial decay is always much faster than the experiments and also the long-time behaviour is not captured.

As a comparison, we also plot (dashed line) the theoretical thermal decay that we derived, see Eq. (2) in the main text, by considering thermal decoherence together with static disorder: as one can see, our predicted decay due to thermal decoherence and static disorder agrees with the experiment much better than modelling the emission intensity neglecting thermal decoherence and considering only static disorder.

At this point, one may wonder whether the agreement at $T = 0$ K with finite disorder
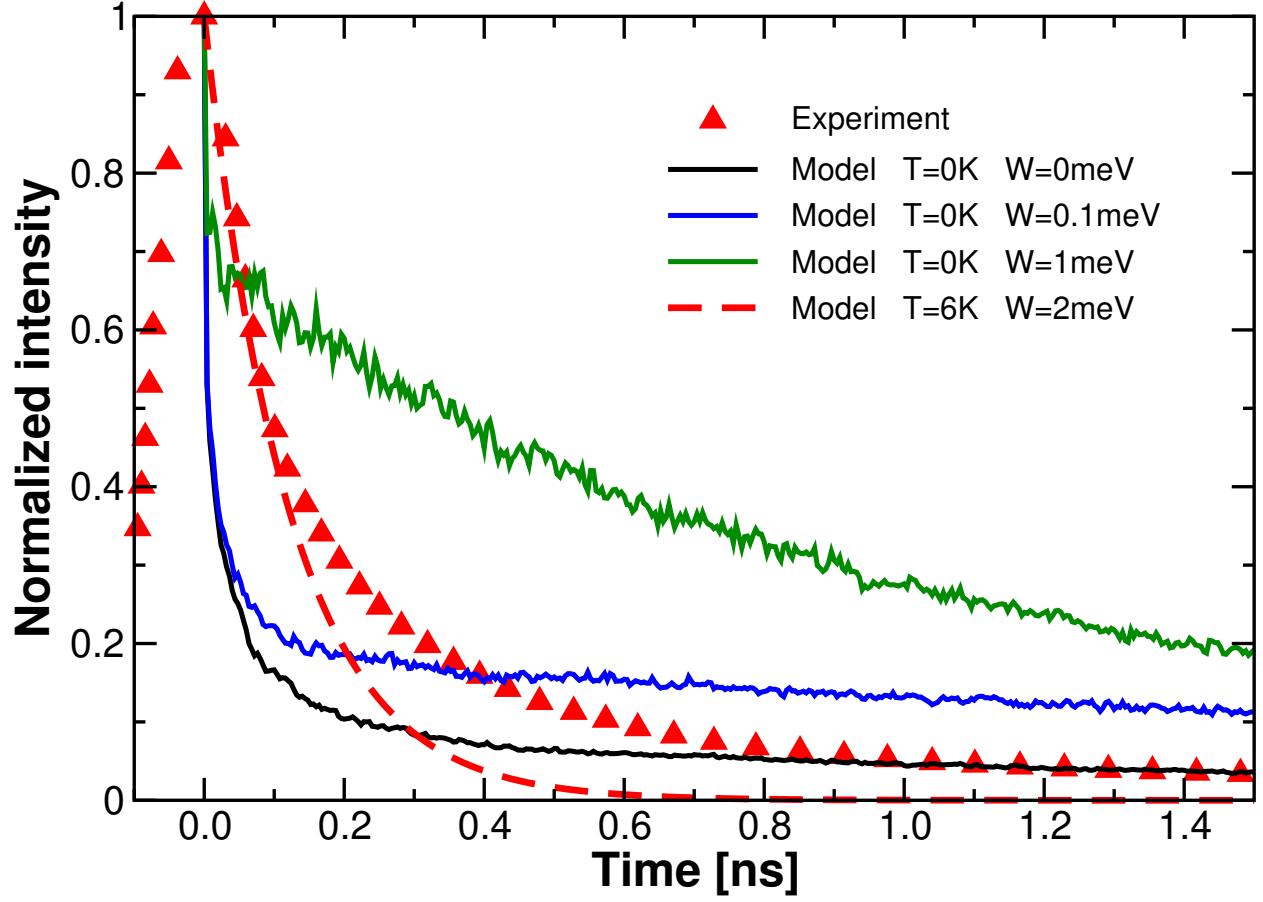
Figure S8: Decay of the emitted intensity in time. Experimental data taken from Ref. 4. Model at $T = 0$ K computed using Eq. (S13) with the Hamiltonian $\hat{H}$ (see Eq. (1) in the main text) corrected as in Eq. (S22). Model at $T = 6$ K computed as discussed in the main text. Parameters: $\hbar\omega_0 = 2.38$ eV, $\gamma_r = 2.5$ ns^{-1}, $\epsilon_r = 4.8$, $N = 1000$, $l = 9$ nm.
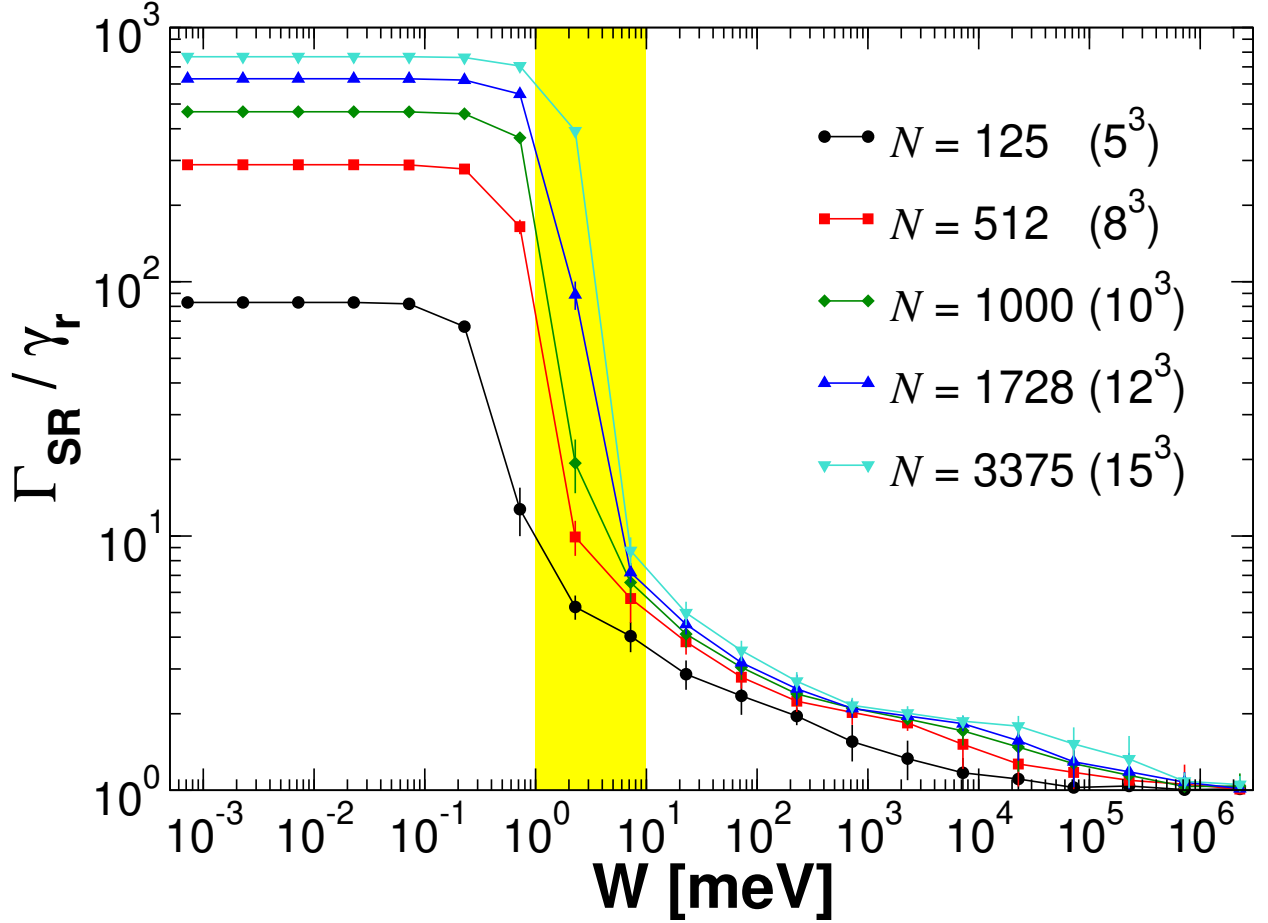
Figure S9: Normalized maximal absolute value of imaginary parts of the complex eigenvalues of $\hat{H}$ for a 3D cubic superlattice *vs.* the amplitude W of the static disorder (see Eq. (S22)), measured in units of $\hbar\gamma_r$. Different values of the number N of nanocrystals are considered (see legend). The yellow region corresponds to a realistic range of disorder. Parameters: $\hbar\omega_0 = 2.38$ eV, $\gamma_r = 2.5$ ns^{-1}, $\epsilon_r = 4.8$ and $l = 9$ nm.

may improve by increasing the system size. Since the initial, fast decay in the model is determined by $\Gamma_{SR} = \max\{\Gamma_k\}$, we analyzed how Γ_{SR} depends on the size for different values of disorder. The results of such analysis are shown in Fig. S9, where Γ_{SR} is plotted against disorder for different values of N. From Fig. S9 one can see that Γ_{SR} tends to γ_r for large W, i.e. SR is quenched by disorder. In the yellow region we mark the range of disorder between 1 meV and 10 meV, that is a realistic estimate of the effective disorder (as discussed in section S10). In such region, we can see that Γ_{SR} increases with N. Therefore, since Γ_{SR} determines the initial decay in Fig. S8, increasing N from 1000 (simulations in Fig. S8) up to $N = 10^6$ would not improve the agreement between the model and the experiments. On the contrary, an extrapolation of the model for large N would increase the overestimation of the initial decay with respect to the experiments. Therefore, we conclude that static disorder alone is not able to explain the quenched SR observed by Rainò et al., and the effect of thermalization needs to be taken into account as explained in the main text and in section S5.

S9   Emission redshift

In the main text (see Fig. 1a) we show that the radiative coupling between NCs results in $3N$ superradiant and subradiant states, whose frequency ω_k is shifted with respect to the single NC emission frequency ω_0. Specifically, the largest redshift in Fig. 1a for $N = 30^3$ is $\sim 700\gamma_r \approx 1$ meV. Here we extrapolate the coupling-induced redshift to natural sizes (up to $N \sim 10^8$) and we compare our predictions with the experimental results.

In Fig. S10 we plot the predicted redshift (symbols) defined as $\max_k[\hbar(\omega_0 - \omega_k)]$ for parameters compatible with Ref. 4. We observe that the redshift predicted by the simulations (symbols) increases slowly with N, following a power law trend $\sim N^{0.2}$ for large N. Once we extrapolate the results to $N = 10^8$, corresponding to the largest superlattices reported in Ref. 4, our model predicts a redshift of at most 7 meV at $N = 10^8$, that is an order of
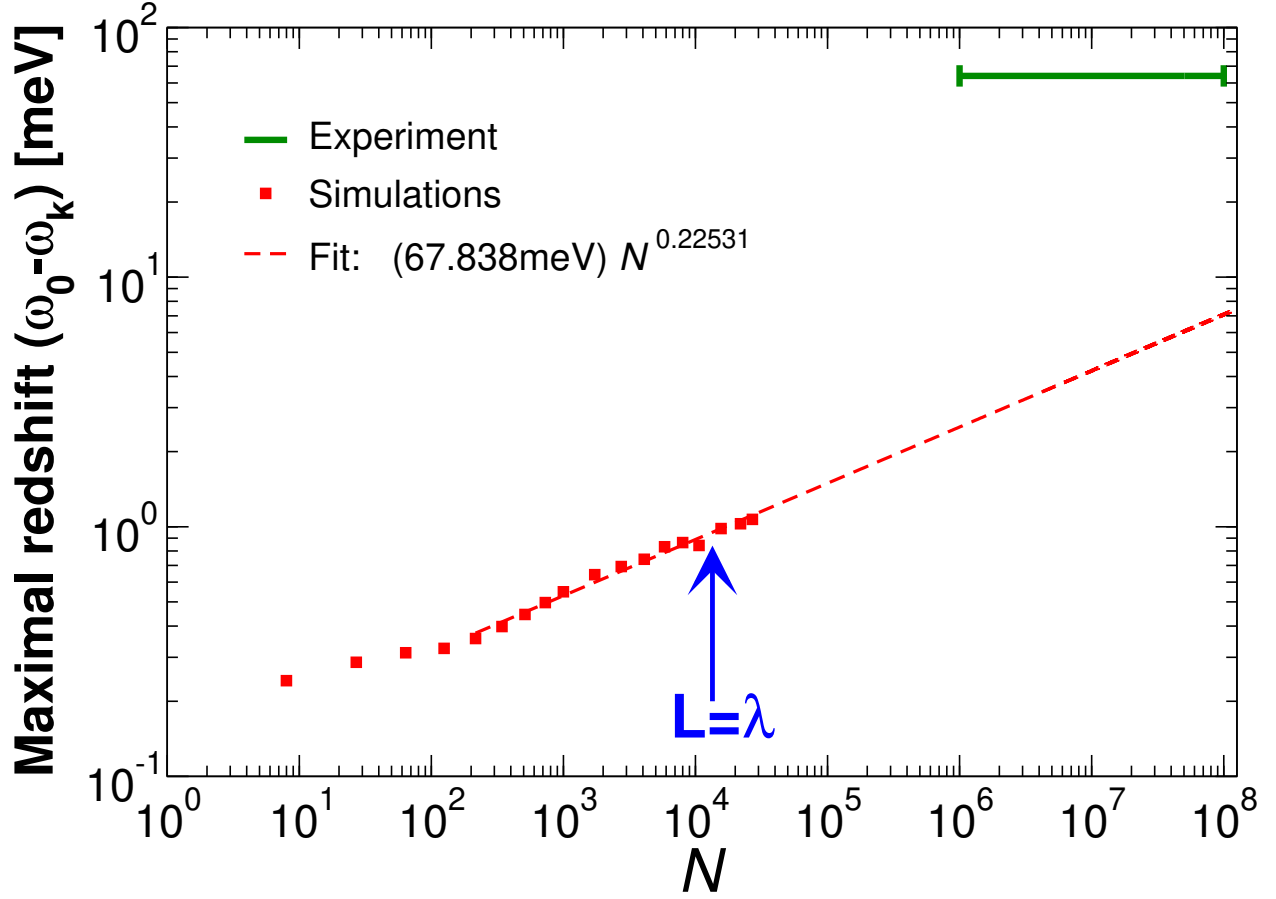
Figure S10: Maximal redshift, $\max_k[\hbar(\omega_0 - \omega_k)]$, with $\hbar\omega_k$ being real part of the eigenvalues of $\hat{H}$ (see Eq. (1) in the main text) and with the NC transition energy $\hbar\omega_0 = 2.38$ eV. The numerical results are fit with a power law and extrapolated to the natural size. "Experiment" refers to the average emission redshift 64 meV reported in Ref. 4. Here, $\gamma_r = 2.5$ ns, $\epsilon_r = 4.8$ and $l = 9$ nm.

magnitude smaller than the average redshift of 64 meV measured experimentally in Ref. 4 averaging over 10 superlattices, see green line for comparison. Consequently there must be another origin to the large redshift observed in Ref. 4.

To begin with, we note that the PL spectrum (at temperature $T = 6$ K) of a single superlattice shown in Fig. 3a of Ref. 4 is composed of two main peaks: one at high energy, with a broad linewidth, assigned to an 'uncoupled' ensemble of NCs, and a second one, narrower and peaked at low energy, that is assigned to a 'coupled' ensemble of NCs. The low-energy 'coupled' peak produces the SR emission. The fact that at least two peaks are visible within the same superlattice can be attributed to the existence of different sub-domains within a single superlattice, as also suggested by Rainò et al. Indeed the existence of several sub-domains, not only two, within a single superlattice is explicitly suggested in Ref. 4 to explain the observation of substructures in the red-shifted emission band. In Ref. 4 it is also stressed that superlattices are made of NCs that are not identical in size, but have a certain size distribution. Another important fact to consider is that $CsPbBr_3$ NCs exhibit strong size-dependent emission.[19] Specifically, in Ref. 19 the emission energy measured at room temperature of $CsPbBr_3$ NCs (reproduced here in Fig. S11a) covers a range of about 300 meV when the side length of the NCs is varied from $l = 3$ nm to $l = 12.8$ nm. The larger NCs possess the lowest, most redshifted emission energy.

Interestingly, from the data reported in Ref. 19, the side length fluctuations are independent of the NCs size, implying that the relative size fluctuations decreases as the NC size increases.

Therefore, we conjecture that the observed large redshifts in Ref. 4 are due to sub-domains made of larger than average NCs, which are more likely to form due to their smaller relative size fluctuations.

The NC size variation reported in Ref. 4 over 100 NCs in Extended Data Fig.1 ranges between 8.5 nm and 10.5 nm, which would cover an excitation energy range of 27 meV according to the data shown in Ref. 19. This contribution, together with the coupling
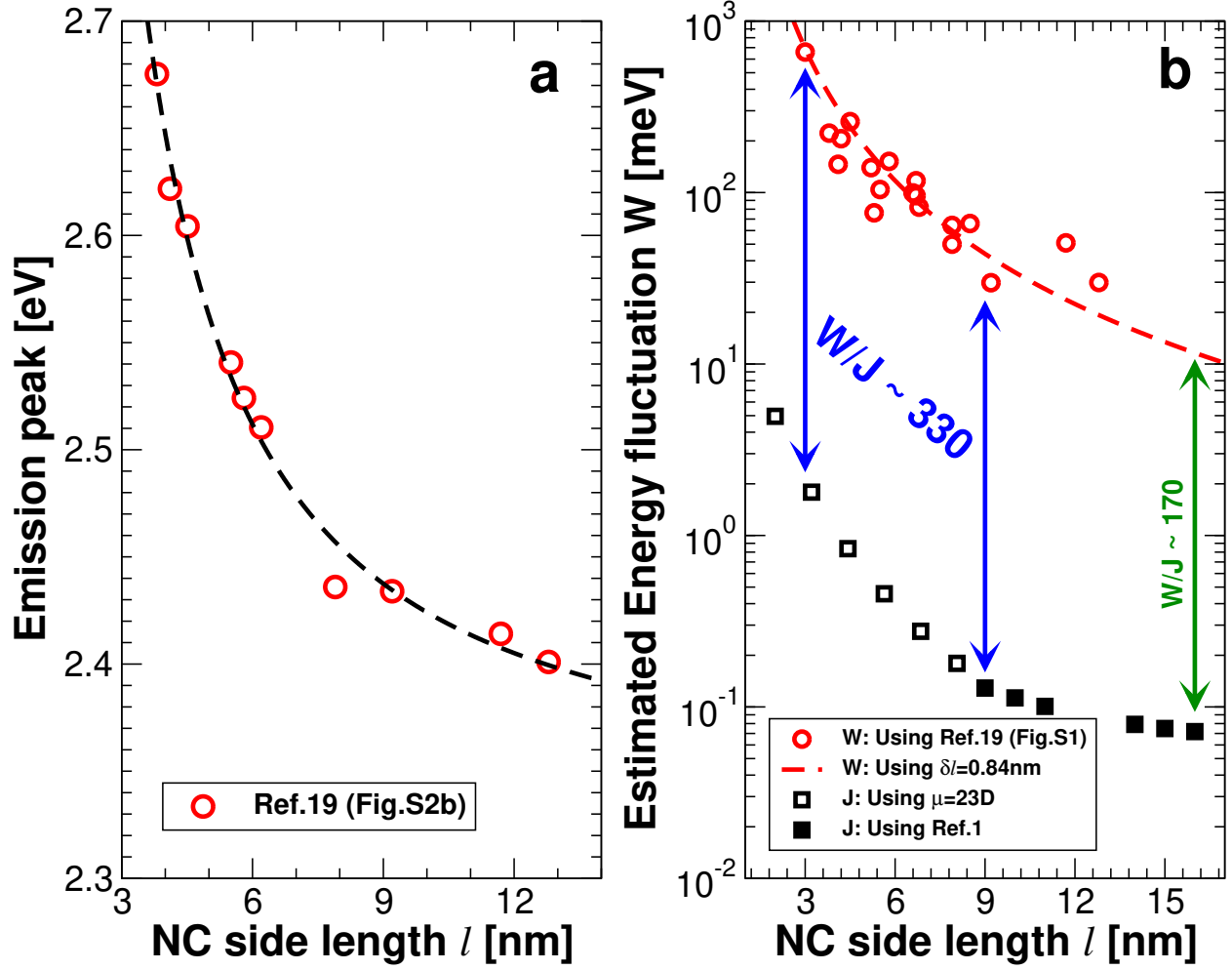
Figure S11: **a** Emission peak for $CsPbBr_3$ NCs of different side length l measured at room temperature (data taken from Ref. 19). The dashed line is the best fit with the function in Eq. (S23). **b** Estimated energy disorder (see Eq. (S25)) against the NC side length using data from Ref. 19 (symbols) and setting a fixed side distribution $\delta l = 0.84$ nm (green dash-dotted line). For comparison, the dipole coupling J between nearest-neighbour NCs is also shown (squares), calculated with two different methods for $l \leq 9$ nm and $l \geq 9$ nm, see text.

contribution of few meV, is only a factor of 2 different from the average observed redshift 64 ± 6 meV. Moreover the size distribution could be larger when the actual number of NCs (10^6-10^8) composing the superlattices is considered. For instance, a size distribution between 8 nm and 12 nm would cover an excitation energy range of about 50 meV, not too far from the observed 64 ± 6 meV redshift.

We stress, however, that the redshift seen in CsPbBr$_3$ NC superlattice emission remains debated with no consensus reached in literature.[20–26] Proposed explanations for such redshifts, which range from 10 meV to 96 meV, include variations in the dielectric constant,[21,25] photon recycling (i.e. reabsorption),[22] electronic coupling between NCs[23] and even bulk CsPbBr$_3$ "impurities".[20]

S10   Static disorder and inhomogeneous linewidth

The emission spectra of SR superlattices reported in Ref. 4 are composed of at least two peaks: a SR redshifted, with an average inhomogeneous linewidth of 15 ± 4 meV, and an additional broader peak, corresponding to an ensemble of uncoupled NCs, with an average inhomogeneous linewidth of 49 ± 21 meV. On the other side, from our theoretical framework (see the main text and details in section S9), we predicted that the amount of disorder present in the SR sub-domain should be of the order of few meV, see Fig. 2a in the main text. This disorder strength cannot explain the inhomogeneous linewidths of the SR peak, that is on average 15 ± 4 meV. In order to explain this large linewidth we note that the existence of several sub-domains, not only two, is explicitly mentioned in Ref. 4: "In most superlattices, we observe a substructure in this red-shifted emission band, which we attribute to the presence of several slightly different independent domains within the same individual superlattice". Thus, we explicitly considered the possibility of having several redshifted sub-domains each composed of NCs of different average sizes. In this way, one could easily explain the inhomogeneous linewidth of few tens of meV as due to different excitation energies

corresponding to the different sizes in each sub-domain. Indeed, $CsPbBr_3$ NC emission energies are strongly size-dependent (see Ref. 19) and the presence of multiple sub-domains within a single superlattice can readily yield an observed 15 ± 4 meV linewidth due to sub-domain induced inhomogeneous broadening.

To corroborate this point, following common theoretical predictions,[1] we fit the measured emission energy obtained from Ref. 19 and reported in Fig. S11a with the function

$$E(l) = \frac{a}{l^2} + \frac{b}{l} + c \, , \tag{S23}$$

obtaining the fit parameters $a = 2.07$ eV nm^2, $b = 0.763$ eV nm and $c = 2.33$ eV. Note that, assuming an SR emission band composed of several NCs sub-domains with mean edge length within 11 nm $< l <$ 13 nm, this would induce an inhomogeneous linewidth of 15 meV, in agreement with the observed inhomogenous linewidth.

Then, from Eq. (S23) we estimate the corresponding energy disorder W for general values of the NC sizes distributed within $(l \pm \delta l)$, where δl is the standard deviation of the side length. Since $\delta l \ll l$, we have

$$\delta E = |E(l + \delta l) - E(l)| \approx \left| \frac{dE(l)}{dl} \right| \delta l = \left| \frac{2a}{l^3} + \frac{b}{l^2} \right| \delta l \, , \tag{S24}$$

where δE represents the standard deviation of the energy fluctuations. Finally, we match the estimated δE parameter (standard deviation) to the model for energy disorder used in this manuscript (see section S8), that entails random energies uniformly distributed within $(\hbar\omega_0 \pm W/2)$. Since the standard deviation in our model is $W/\sqrt{12}$, we obtain

$$W \approx \sqrt{12} \left| \frac{2a}{l^3} + \frac{b}{l^2} \right| \delta l \, . \tag{S25}$$

In Fig. S11b the estimated energy disorder (see Eq. (S25)) is plotted against the NC side length using values of $(l, \delta l)$ reported in Ref. 19 (symbols). As one can see, the estimated

energy disorder W ranges between ~ 20 meV and ~ 700 meV, with the smallest energy disorder corresponding to the largest NCs. Also, the NC size fluctuations from Ref. 19 are independent of l, so that we evaluate Eq. (S25) using the average size fluctuations $\delta l = 0.84$ nm from Ref. 19 (red dashed line in Fig. S11b) and we capture well the dependence between W and l. Note that the measurements in Ref. 19 were done at room temperature, while disorder is likely smaller at lower temperatures.

The conjecture of multiple redshifted sub-domains necessitates that in each sub-domain with SR emission, W cannot be larger than few meV to allow for SR emission to be observed, see Fig. 2a in the main text. This implies that sub-domains with SR emission should be characterized by a highly uniform size distribution which would favor the formation of a coherent sub-domain and it would allow to observe coherent emission.

Note that, since thermal decoherence occurs on few picoseconds timescales,[17] while emission occurs on few hundreds of picoseconds, thermal decoherence cannot be neglected. Taking thermal decoherence into account implies that each sub-domain should be composed of at least $\sim 10^4$ NCs, see Fig. 2a in the main text.

In whole, the existence of SR sub-domains, where each sub-domain is composed of large NCs, with an average size differing from sub-domain to sub-domain, self-consistently rationalizes three observations made in Ref. 4: (1) unexpected $\approx 64 \pm 6$ meV redshifts, (2) large $\approx 15 \pm 4$ meV SR inhomogeneous linewidths and (3) SR emission spectral substructure.

We also note that the predicted energy disorder increases as l is decreased (with δl independent of l). This may induce to think that small-l superlattices would be more sensitive to disorder, compared to their large-l counterparts. However, also the dipole coupling between nearest-neighbour NCs within a superlattice increases for small l (see black symbols in Fig. S11b). Here, following Ref. 1, we compute the nearest-neighbour coupling $J \approx \mu^2/(l')^3$ accounting for the dependence of the TDM μ on the NC size. In the strong confinement regime ($l \ll 2a_B$, where a_B is the exciton Bohr radius) the TDM is independent from the NC side length, therefore here we use a constant TDM $\mu = 23$ D for $l \leq 9$ nm (open black

squares in Fig. S11b). In the opposite regime (weak confinement, $l \gg 2a_B$) the calculated TDM scales as $\mu^2 \sim l^3$, implying that J is independent of the NC size for very large l. Finally, in the intermediate confinement regime (that we identify as 9 nm $\leq l \lesssim 16$ nm) we extract μ for the different NC sizes from Ref. 1. Then we use μ to compute $J \approx \mu^2/(l')^3$ and we multiply the coupling obtained this way by a factor 1.3 to match the data at $l = 9$ nm reported in Ref. 4, see filled black squares in Fig. S11b.

Since both W and J scale as $1/l^3$ for small l (see Eq. (S25)) and μ is constant in such regime (as explained above), the ratio W/J is constant for $l \leq 9$ nm. Given that the effect of disorder is determined by the ratio W/J, we conclude that the effect of disorder on SR is independent of the NC size, for $l \lesssim 9$ nm. Note that the disorder values in Fig. S11b are much larger than the disorder estimated in Fig. 2a of the main text, i.e. $W/J \approx 15$. One possible reason for such discrepancy is that in Fig. S11b we use data measured at room temperature,[19] while in Fig. 2a of the main text we compare to experiments at $T = 6$ K, where a smaller disorder is expected. Moreover, as we conjecture in the main text and in section S9, the SR emission likely comes from very ordered, homogeneous sub-domains within the superlattice. The size distribution within such sub-domains is likely much smaller than 0.84 nm, rationalizing the smaller disorder $W/J \approx 15$ in Fig. 2a. Therefore, since disorder has a minor effect for NC sizes of $l = 9$ nm with $W/J \approx 15$ (as shown in Fig. 2a in the main text), the same minor effect could be expected for smaller NC sizes, provided that the size fluctuations can be controlled in order to keep the same ratio W/J.

On the other hand, if the size fluctuations could not be controlled for small NCs, disorder could be so large to completely quench SR. In such case, an alternative way to observe SR is to use large NCs ($l \gtrsim 9$ nm). In such regime the coupling J tends to a constant value, as discussed above (see black filled squares in Fig. S11b), while W always decreases with the NC size. Therefore the ratio W/J decreases for large NC sizes as shown in Fig. S11b, where W/J is nearly halved varying l from 9 nm to 16 nm. An even smaller reduction of W/J is expected for larger NCs, for example for $l = 25$ nm, J is expected to saturate above

$l = 16$ nm, see Fig. S11b), and we would obtain a value of W/J, 5 times smaller than the its value for $l \leq 9$ nm. However, note that large NCs have couplings J weaker than small NCs (compare empty and filled black squares in Fig. S11b), so that smaller NCs are always more robust to thermal decoherence.

Supporting References

(1) Becker, M. A.; Vaxenburg, R.; Nedelcu, G.; Sercel, P. C.; Shabaev, A.; Mehl, M. J.; Michopoulos, J. G.; Lambrakos, S. G.; Bernstein, N.; Lyons, J. L., et al. Bright triplet excitons in caesium lead halide perovskites. *Nature* **2018**, *553*, 189–193.

(2) Bellando, L.; Gero, A.; Akkermans, E.; Kaiser, R. Cooperative effects and disorder: A scaling analysis of the spectrum of the effective atomic Hamiltonian. *Phys. Rev. A* **2014**, *90*, 063822.

(3) Bettles, R. *Cooperative interactions in lattices of atomic dipoles*; Springer, 2017.

(4) Rainò, G.; Becker, M. A.; Bodnarchuk, M. I.; Mahrt, R. F.; Kovalenko, M. V.; Stöferle, T. Superfluorescence from lead halide perovskite quantum dot superlattices. *Nature* **2018**, *563*, 671–675.

(5) Ashcroft, N. W.; Mermin, N. D. *Solid state physics*; Holt, Rinehart and Winston, 1976.

(6) Vovk, I. A.; Tepliakov, N. V.; Baimuratov, A. S.; Leonov, M. Y.; Baranov, A. V.; Fedorov, A. V.; Rukhlenko, I. D. Excitonic phenomena in perovskite quantum-dot supercrystals. *Phys. Chem. Chem. Phys.* **2018**, *20*, 25023–25030.

(7) Madjet, M. E.; Abdurahman, A.; Renger, T. Intermolecular Coulomb Couplings from Ab Initio Electrostatic Potentials: Application to Optical Transitions of Strongly Coupled Pigments in Photosynthetic Antennae and Reaction Centers. *The Journal of Physical Chemistry B* **2006**, *110*, 17268–17281.

(8) Brus, L. E. Electron–electron and electron-hole interactions in small semiconductor crystallites: The size dependence of the lowest excited electronic state. *The Journal of Chemical Physics* **1984**, *80*, 4403–4409.

(9) Grad, J.; Hernandez, G.; Mukamel, S. Radiative decay and energy transfer in molecular aggregates: The role of intermolecular dephasing. *Phys. Rev. A* **1988**, *37*, 3835–3846.

(10) Meiser, D.; Holland, M. J. Steady-state superradiance with alkaline-earth-metal atoms. *Phys. Rev. A* **2010**, *81*, 033847.

(11) Zhu, B.; Schachenmayer, J.; Xu, M.; Herrera, F.; Restrepo, J. G.; Holland, M. J.; Rey, A. M. Synchronization of interacting quantum dipoles. *New Journal of Physics* **2015**, *17*, 083063.

(12) Hestand, N. J.; Spano, F. C. Expanded theory of H-and J-molecular aggregates: the effects of vibronic coupling and intermolecular charge transfer. *Chem. Rev.* **2018**, *118*, 7069–7163.

(13) Gullì, M.; Valzelli, A.; Mattiotti, F.; Angeli, M.; Borgonovi, F.; Celardo, G. L. Macroscopic coherence as an emergent property in molecular nanotubes. *New Journal of Physics* **2019**, *21*, 013019.

(14) Meier, T.; Zhao, Y.; Chernyak, V.; Mukamel, S. Polarons, localization, and excitonic coherence in superradiance of biological antenna complexes. *The Journal of Chemical Physics* **1997**, *107*, 3876–3893.

(15) Breuer, H. P.; Petruccione, F. *The theory of open quantum systems*; Oxford University Press: Great Clarendon Street, 2002.

(16) Sakurai, J. J. *Modern quantum mechanics, revised edition*; Addison-Wesley Publishing Company, 1995.

(17) Brennan, M. C.; Forde, A.; Zhukovskyi, M.; Baublis, A. J.; Morozov, Y. V.; Zhang, S.; Zhang, Z.; Kilin, D. S.; Kuno, M. Universal Size-Dependent Stokes Shifts in Lead Halide Perovskite Nanocrystals. *The Journal of Physical Chemistry Letters* **2020**, *11*, 4937–4944.

(18) Celardo, G. L.; Giusteri, G. G.; Borgonovi, F. Cooperative robustness to static disorder: Superradiance and localization in a nanoscale ring to model light-harvesting systems found in nature. *Phys. Rev. B* **2014**, *90*, 075113.

(19) Brennan, M. C.; Herr, J. E.; Nguyen-Beck, T. S.; Zinna, J.; Draguta, S.; Rouvimov, S.; Parkhill, J.; Kuno, M. Origin of the Size-Dependent Stokes Shift in CsPbBr3 Perovskite Nanocrystals. *Journal of the American Chemical Society* **2017**, *139*, 12201–12208.

(20) Baranov, D.; Toso, S.; Imran, M.; Manna, L. Investigation into the Photoluminescence Red Shift in Cesium Lead Bromide Nanocrystal Superlattices. *The Journal of Physical Chemistry Letters* **2019**, *10*, 655–660.

(21) van der Burgt, J. S.; Geuchies, J. J.; van der Meer, B.; Vanrompay, H.; Zanaga, D.; Zhang, Y.; Albrecht, W.; Petukhov, A. V.; Filion, L.; Bals, S.; Swart, I.; Vanmaekelbergh, D. Cuboidal Supraparticles Self-Assembled from Cubic CsPbBr3 Perovskite Nanocrystals. *The Journal of Physical Chemistry C* **2018**, *122*, 15706–15712.

(22) Nagaoka, Y.; Hills-Kimball, K.; Tan, R.; Li, R.; Wang, Z.; Chen, O. Nanocube Superlattices of Cesium Lead Bromide Perovskites and Pressure-Induced Phase Transformations at Atomic and Mesoscale Levels. *Advanced Materials* **2017**, *29*, 1606666.

(23) Tong, Y.; Yao, E.-P.; Manzi, A.; Bladt, E.; Wang, K.; Döblinger, M.; Bals, S.; Müller-Buschbaum, P.; Urban, A. S.; Polavarapu, L.; Feldmann, J. Spontaneous Self-Assembly of Perovskite Nanocrystals into Electronically Coupled Supercrystals: Toward Filling the Green Gap. *Advanced Materials* **2018**, *30*, 1801117.

(24) Imran, M.; Ijaz, P.; Baranov, D.; Goldoni, L.; Petralanda, U.; Akkerman, Q.; Abdelhady, A. L.; Prato, M.; Bianchini, P.; Infante, I.; Manna, L. Shape-Pure, Nearly Monodispersed CsPbBr3 Nanocubes Prepared Using Secondary Aliphatic Amines. *Nano Letters* **2018**, *18*, 7822–7831.

(25) Kovalenko, M. V.; Bodnarchuk, M. I. Lead halide perovskite nanocrystals: From discovery to self-assembly and applications. *CHIMIA International Journal for Chemistry* **2017**, *71*, 461–470.

(26) Wang, K.-H.; Yang, J.-N.; Ni, Q.-K.; Yao, H.-B.; Yu, S.-H. Metal Halide Perovskite Supercrystals: Gold–Bromide Complex Triggered Assembly of CsPbBr3 Nanocubes. *Langmuir* **2018**, *34*, 595–602.